Effects of particle size on the pyrolysis of spruce and poplar: Thermogravimetric analyses, DAEM modelling, validation, and prediction of secondary charring

Yong Tian, Patrick Perré

Graphical Abstract

Experiments with different particle sizes

Learning database with dynamic tests

TGA kinetics

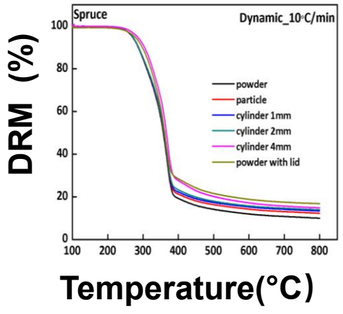

Elemental analyses

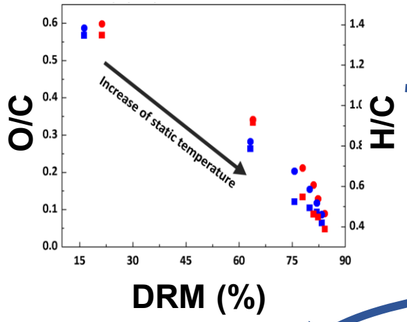

Validation database with static tests

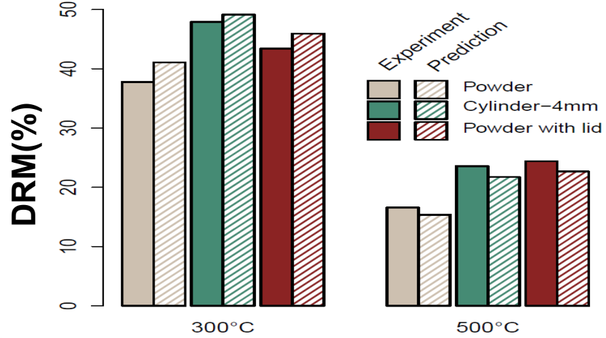

DAEM modelling

2 Gaussian + 1 exponential distributions

Prediction of kinetics differences

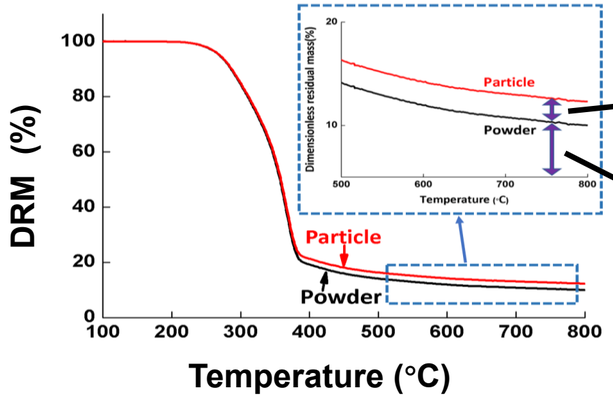

Secondary charring (mainly carbon)

Powder C, H and O = functions of DRM

Prediction of elemental composition

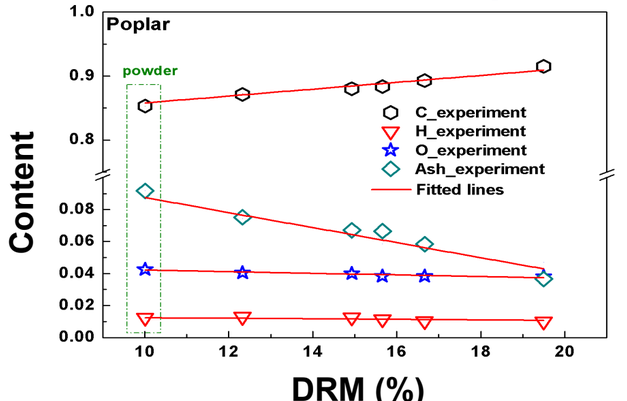

Highlights:

(1) Multiple sample geometries revealed effects of particle size on char formations

(2) A negative carbonization / mass loss correlation occurred while increasing particle size

(3) Synthetic indexes built from model parameters depicted kinetic differences

(4) Model's prediction ability regarding particle sizes was validated

(5) Strategy proposed to predict char compositions for a given size at any temperature-time pathway

Effects of particle size on the pyrolysis of spruce and poplar: thermogravimetric analyses, DAEM modelling, validation, and prediction of secondary charring

Yong TIAN[a,b*], Patrick PERRÉ[a,b]

[a] LGPM, CentraleSupélec, Université Paris-Saclay, 3 Rue Joliot Curie, 91190 Gif-sur-Yvette, France

[b] LGPM, Centre Européen de Biotechnologie et de Bioéconomie (CEBB), 3 Rue des Rouges Terres, 51110, Pomacle, France

[*]Corresponding author.

E-mail address: tianyong_2021@126.com (Yong TIAN), patrick.perre@centralesupelec.fr (Patrick Perré)

Abstract:

Particle size plays a crucial role in biomass pyrolysis mechanisms and their subsequent industrial uses. However, an applicable kinetic method that combines thermogravimetric data with distributed activation energy model (DAEM) adapted to the sample size is still missing. This work investigated pyrolysis kinetics of two wood species (spruce and poplar) with five particle shapes (powder, particle, 5-mm diameter cylinders with heights of 1 mm, 2 mm, and 4 mm) and one additional reaction condition (powder with lid). The experimental data were numerically simulated by two Gaussian + one exponential DAEM distributions. Thermogravimetric results evidenced a significant effect of particle geometry on char yields, which increased by 81% and 66%, from powder to 4-mm high cylinders, for spruce and poplar respectively. The increase in particle size and use of a crucible lid led to an increase of exothermic heat. Elemental analysis demonstrated a contradictory relation between

carbonization and mass loss, which was explained by secondary charring. Synthetic indexes built from the kinetics parameters of the DAEM model clearly depicts the effect of particle sizes. The prediction ability of the model was checked by further experiments performed at different time-temperature patterns with several particle sizes. Finally, correlations between dimensionless residual mass (DRM) and element compositions allowed us to determine the composition of secondary charring, which consists mainly of carbon. The elemental composition of char can therefore be predicted using the difference of DAEM kinetics between fine powder and a given particle size.

Keywords: Biomass; Elemental analysis; Particle size; Pseudo-component; Wood.

1. Introduction

Lignocellulosic biomass is an important renewable energy source for the worldwide energy supply. Its large deposits and carbon neutrality offer an enormous potential to meet future energy demands and reduce environmental pollutions [1]. Pyrolysis is part of the thermochemical route to convert biomass into high value-added chemical products: bio-oil, charcoal, and gaseous fuels. It is the initial step before further thermochemical technologies such as combustion and liquification, making pyrolysis a key link in the BtL (biomass to liquid) industrial chain and subsequent exploitation. Process factors including temperature, heating rate, particle size, and residence time could effectively alter product categories and yields [2-4]. Among them, the particle size specifically affects the pyrolysis mechanism in relation to volatile interaction, mass, and heat transport, which imposes strict requirements on industrial reactors [5]. Therefore, both experimental and theoretical kinetic works are necessary to determine and predict the effect of particle size.

A considerable number of studies have been conducted to test the effect of particle size on biomass pyrolysis. As well acknowledged, mass and heat transfer were severely affected in large particles (>1.5mm) during both pyrolysis experiments and modeling [6]. Di Blasi [7] calculated that, in terms of thermal transfer, particle size affects the internal heating rate in fast pyrolysis, which decreased from 760 °C /s to 23 °C /s when the particle diameter was increased from 0.1 mm to 1 mm. Okekunle [8] found the intra-particle temperature gradient increased with particle size and aspect ratio, which promoted intra-particle char formation. Perré and co-workers [9, 10] developed comprehensive computational models that emphasized the effect of particle size or particle beds on the evolutions of the temperature profiles, with opposite effects in the heating period and during the reaction period due to exothermic reactions. A model developed by Anshu [11] claimed more devolatilization delay occurred in larger biomass samples because of intra-particle transfer retardation. Suriapparao [12] and Acma [13] claimed higher apparent activation energy with increasing particle size due to mass transfer limitation and the intra-particle thermal gradient.

It was well-accepted that the increasing non-isothermal processes in large particles led to low oil and high char yields [14, 15]. Shen [16] postulated that a decreased heating rate in large particles was primarily responsible for lower bio-oil yield, and the fiber destruction in small particles favored high oil yield. Ayhan [17] observed the reduction in char yield when imposing high heating rate in small particles. Zhou [18] proved that physical trapping of thermally ejected oligomers occurred as a function of particle size, from milled particles (0.3–0.55 mm) to cylinders (3–14 mm). Westerhof [19] argued that physical retainment of vapors or aerosols caused excessive volatile condensation in large particles and cylinders.

With an increase in particle size, the added cellular- and tissue-scale barriers have an increasing impact on pyrolysis [20]. More specifically, their effects originated from two parts: (1) different degrees of destruction of fiber structures in milled particles; and (2) different

dimensions in an integral cylinder or chip. In the first scenario, milled samples lose most typical wood channel structures. Small particles usually impose less resistance on both heat and mass transfer profiles due to their microstructures; tissue expansion and lumina cell wall stretch are therefore less restricted [20], leading to easier volatile release. For the second scenario, geometry differences in cylinders cause hermetic spaces and anisotropic channels that can obstruct internal volatilization to varying degrees, and the vapor outflow pattern is largely affected by internal heat transfer limitations [19]. The increase of particle size, in this case, delays volatile's escape inside the material matrix and offers additional possibilities for secondary charring. Moreover, axial conductivity values have been found to be three times larger for thermal transfer and fifteen times larger for mass transfer than their corresponding radial conductivity values [21], larger anisotropic degree in the cylinder leads to significant temperature gradients and flow gradients, generally causing volatile blockage and char generation [22].

Particle size clearly linked with the extent of secondary reactions, which usually occur in two competitive pathways: charring and cracking, causing carbon deposition and gas production, respectively. As long residence time of volatiles in high-temperature zone favors polymerization and carbonization, the reduction of heating rate inhibits the complete vaporization [23], and high pressure stimulates carbonization by concentrating the vapor phase [24]. All these process parameters help secondary charring prevail over cracking. Meanwhile, other factors such as chemical compositions, density, and the presence of inorganics (alkali metals) also influence charring reactions by different mechanisms [25, 26]. In contrast, secondary cracking converts volatiles into small molecular gases, which normally accompanies with short residence times, high heating rates, or dilute vapor phases [27]. Regarding the main constituents of biomass, hemicellulose undergoes charring through rearrangement reactions of polysaccharides and further demethylation [28]; cellulose

undergoes secondary charring by the oligomerization of primary pyrolysis product: levoglucosan [29]; lignin is a fine charring precursor due to its original high aromatic ring content, whose short substitutes cleaves increase the aromaticity and reticulation in the residue over the temperature range of 500–800 °C [28].

It is worthwhile to investigate the effect of particle size from the angle of kinetic models, which can be potentially applied in complicated multi-scale simulations and operational controls in industrial processes [30]. The DAEM is an efficient and robust approach to represent the kinetics of complex decomposition reactions [31], and at present, is widely used to model the biomass pyrolysis [32, 33]. The model assumes that biomass pyrolysis occurs as a series of independent and parallel reactions with continuous activation energy distributions, representing the variability of interactions due to complex macromolecular structures and their interactions in the cell wall [34]. Three-parallel-distribution DAEM presents an even more accurate approach to the description of the pyrolysis kinetics of various lignocellulosic biomasses [35-37], and the interpretation of pseudo-components as chemical constituents (hemicellulose, cellulose, and lignin) is justified as a useful method in kinetic research [38-40]. The kinetic additivity of the three main constituents provides universal applicability for various biomass species [41], being crucial for single-particle reaction kinetics as well as large-scale process implementations. However, the nature of devolatilization theory in the DAEM formulation makes it difficult to account for recondensation and secondary charring reactions among different particle sizes or shapes. To our best knowledge, DAEM has rarely been applied to distinguish the effects of particle size; furthermore, the three-distribution DAEM has never been employed to distinguish the kinetics of different particle sizes. The two Gaussian + one exponential DAEM was recently proved to be very efficient in handling multiple temperature profiles and complex heat fluxes,

including at the validation stage [42]. Hence, this model was applied in the present work to analyze the pyrolysis kinetics of different particle sizes.

This study aims to investigate the effects of particle size by coupling thermogravimetric kinetics and numerical methods. Thermogravimetry (TG) and differential scanning calorimetry (DSC) will be performed at two heating rates for a wide range of particle sizes. Elemental analyses will demonstrate that the relation between carbonization and mass loss is directly linked to the particle size. Further, Synthetic indexes will be built from the kinetics parameters of the three-distribution-DAEM model to clearly depict the effect of particle sizes. Importantly, the prediction ability of the model will be validated using an additional set of experiments performed with different temperature pathways: a linear increase of temperature followed by a plateau at constant temperature (different temperature levels will be performed). Finally, correlations between mass loss (ML) and element compositions will allow us to determine the composition of secondary charring. This composition will be used to predict the elemental composition of char for a given particle size.

2. Material and methods

2.1 Material

One gymnosperm and one angiosperm species were used in this study: European spruce (*Picea abies*, softwood, 450 kg/m^3, cut from a 73-year-old tree grown in the forest in the Auvergne region, France) and poplar (*Populus euroamericana* 'Koster', hardwood, 364 kg/m^3, cut from a 25-year-old tree grown in the forest in La Suippe Valley in la Marne, France). The complete sample preparation protocol is depicted in Figure 1. Second-bottom tree logs (2 m long, cut at 2 m high above the ground) of 40–50 cm diameter were used. They were cut evenly into 2.5 cm-thick boards, and the one 10 cm from the pith was taken for the

present study. Rectangular sticks of 2.5 cm × 2.5 cm × 20 cm (length × width × height) were cut from a healthy sapwood part of the board to ensure uniform properties. The stick was further processed into cylinders with a diameter of 5 mm and a length of 3 cm by a lathe (PROMAC 961V), then cut into regularly shaped cylinders by a precision cut-off machine (Struers, Secotom-15) with two successive sequences of 1 mm, 2 mm, and 4 mm. The rest of the stick was ground with an M20-IKA universal mill, then put into sieve stacks of 0.063 mm, 0.08 mm, 0.63 mm, and 0.8 mm opening sizes on a vibratory sieve shaker (RETSCH AS 200) at 90% amplitude for 30 minutes. The sieving cut between 0.063–0.08 mm was taken as wood powder, and the cut between 0.63–0.8 mm was taken as wood particles. The strict protocol defined here intended to limit any difference in composition between all types of samples and to constrain the size of the small particles. Therefore, it was reasonable to assume that differences in pyrolysis behavior were derived exclusively from the particle geometry. After the preparations, all samples were dried at 105 °C in an oven for 24 h and stored in a desiccator.

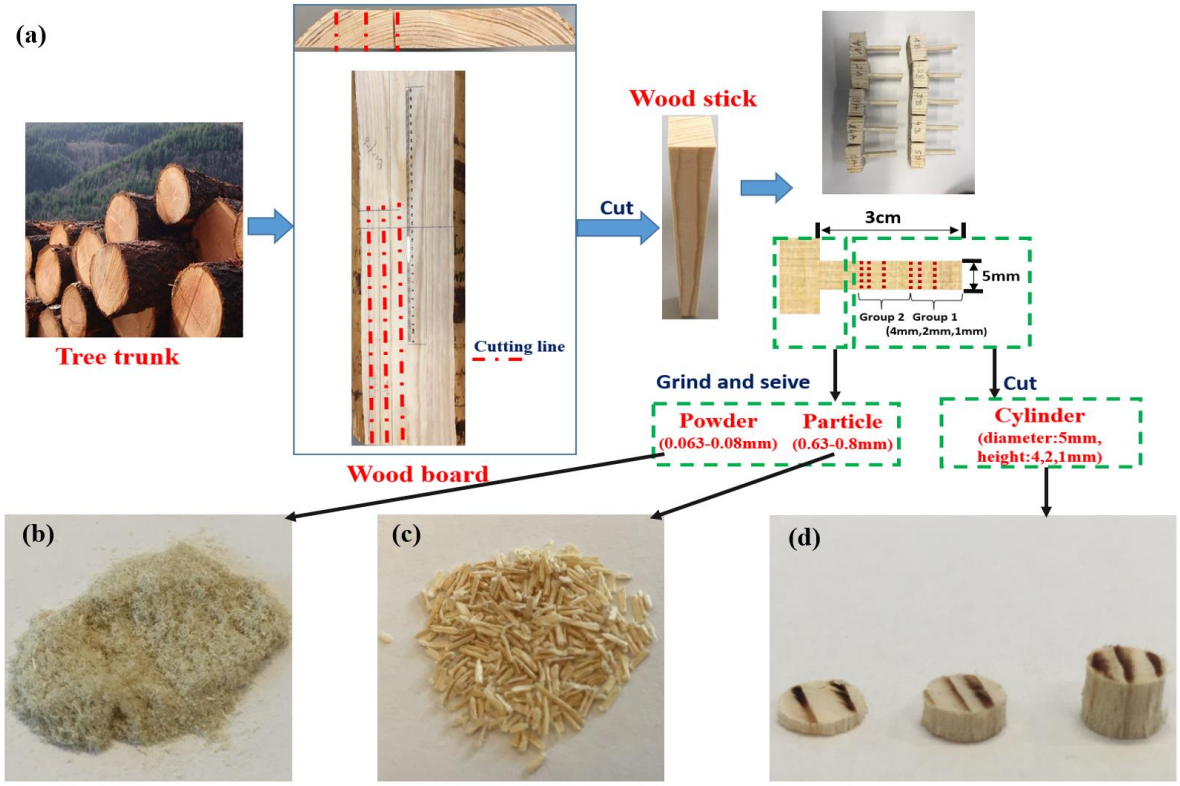

Figure 1. (a) Flow chart of the preparation protocol of the wood samples; and pictures of three scales of samples (using spruce as an example): (b) powder, (c) particles, and (d) cylinders.

Ultimate and proximate analyses were conducted in a Thermo Fisher Scientific FLASH 2000 organic elementary analyzer and a Nabertherm LV/9/11 furnace, respectively, by the standards ASTM E1755 and E872. The basic chemical properties of two types of wood on a dry basis are shown in Table 1.

Table 1. Proximate and ultimate analysis of spruce and poplar

Biomass type	Proximate analysis (wt.%)			Ultimate analysis (wt.%)		
	Volatile	Ash	FC	C	H	O
Spruce	84.93	0.29	14.78	47.07	5.97	43.65
Poplar	86.29	0.37	13.34	48.06	5.95	43.76

All samples' microstructures had been visualized (photos could be found in supporting material). Powder and particles were analyzed by environmental scanning electron microscopy (ESEM, FEI Quanta electron microscope), and cylinders were examined using 3D X-ray tomography (RX Solutions EasyTom XL Ultra 150-160) with a spatial resolution of 3μm. For both spruce and poplar, the differences in microstructure between the different particle sizes were obvious. As shown in the Supplementary Figure 1, the powder presented broken, fragmented pieces, with damaged lumens and inner cell wall structures were largely exposed. Particle samples preserved the cellular structure of wood: cells retained partial intact structures and exposed lumens at the edges. As expected, wood cylinders maintained the original anatomical structure of wood. Spruce, despite obvious annual rings, had a uniform anatomical pattern that consisted mainly of tracheids. As a diffuse ring-porous hardwood, poplar presented two contrasting sizes of pore: vessels and fibers.

2.2 Experimental method

Wood pyrolysis was carried out in a thermogravimetric analyzer (STA 449 F3 Jupiter, NETZSCH). Thermal gravimetric (TG) and differential scanning calorimetry (DSC) signals were simultaneously acquired at a time interval of 0.1 min. Measurements were conducted under a nitrogen purge (99.999%) of 50 ml/min and a protective gas flow of 20 ml/min. Dynamic tests at two heating rates (1 °C/min and 10 °C/min) were applied for all wood samples. The program began by heating the sample from 30 °C to 100 °C at 10 °C/min and was held for 30 minutes to eliminate the residual water in sample. Then the temperature was increased from 100 °C to 800 °C at the aforementioned heating rates. Finally, the temperature dropped to 30 °C with unchanged nitrogen sweeping. Additional tests with a pierced lid (central hole of 0.5 mm) were also performed with biomass powder. Therefore, three particle

geometries: powder, particles, and cylinders (heights: 1 mm, 2 mm, and 4 mm) together with another type of reactor (crucible with lid) resulted in six sample configurations performed for spruce and poplar at two heating rates. In addition, static tests were performed for validation purposes. Their temperature programs began with the same sequence, heating powder samples from 30 °C to 100 °C at 10 °C/min and holding for 30 minutes. Then the temperature was raised at a rate of 10 °C/min to the plateau temperature (from 250 °C to 500 °C by an increment of 50 °C plus one test at 800 °C). The plateau temperature was maintained for 2 h, followed by cooling to 30 °C with unchanged nitrogen sweeping.

Temperature and sensitivity calibrations were performed specific to crucible type, temperature rate, and gas type. The certified standards (NETZSCH calibration set) include indium, tin, bismuth, zinc, aluminum, and silver. The accuracy of the DSC signal was also checked with sapphire, according to the NETZSCH handbook. Blank tests were conducted before every sample test with the same crucible to keep the same buoyancy effects and ensure the same heat capacity. Dimensionless residual mass (DRM) and conversion rate (X_{exp}) were used to process TG signals:

$$DRM(t) = m_t/m_0 \times 100\%, \quad X_{exp}(t) = 1 - DRM(t) \tag{1}$$

where m_t is the remaining mass at time t, and m_0 is the anhydrous mass after the 30-minute plateau at 100 °C.

2.3 DAEM formulation

DAEM calculates the volatile contributions from parallel and irreversible first-order reactions. The integral form of conversion degree, $X(t)$, could be expressed as:

$$X(t) = V(t)/V^{\infty} = 1 - \int_0^{\infty} exp\left(-\int_{t_0}^{t} A_0 e^{-E/RT(t)} dt\right) f(E) dE \tag{2}$$

where V^{∞} is the theoretical total volatile amount, $V(t)$ is the volatile production at time t, and E is the activation energy. The important assumption of keeping pre-exponential factors of all reactions as a constant, A_0, has been justified by the accurate identification and model concision [42, 43], and similar concept had been accepted and applied in relevant researches [44-46]. R is the universal gas constant and $T(t)$ is the temperature at time t. $f(E)$ is the statistical function for describing the activation energy distribution.

Wood is treated as an aggregate of three pseudo-components based on the assumptions that no interactions exist during pyrolysis, and they correspond to three distributions ($f_j(E)$) with different weighting factors $V_{max}(j), (j = 1,2,3)$. The final formulation of biomass conversion degree is therefore expressed as:

$$X(t) = 1 - \sum_{j=1}^{3} V_{max}(j) \int_0^{\infty} exp\left(-A_0 \int_0^t e^{-E/RT(t)} dt\right) f_j(E) dE \quad (3)$$

In this work, two Gaussian and one exponential distributions are chosen for its excellent trade-off between accuracy and model conciseness [43]. Two Gaussian distributions are used to represent the first and second pseudo-components. They are formulated using the mean activation energy E_0 and standard deviation σ as:

$$f(E) = \frac{1}{\sigma\sqrt{2\pi}} \exp\left(-\frac{(E - E_0)^2}{2\sigma^2}\right) \quad (4)$$

The third pseudo-component is represented by an exponential distribution, one degeneracy form of the gamma distribution:

$$f(E) = \beta exp\left(-\beta \frac{E - E_{min}}{E_{min}}\right) \quad (5)$$

where β is the rate parameter and E_{min} the minimum activation energy. The integral term of equation (3) demands further numerical discretization for each type of distribution, which has been presented in detail in our recent works [42, 43]. High temperature level and

wide range of activation energy might cause small characteristic time. For better accuracy in numerical integration, the effective approximation value of chemical reaction dV_i over the time step is therefore expressed in its original exponential form [47, 48]:

$$dV = \sum_{j=1}^{3}\sum_{i=1}^{N_p}\left[1 - exp\left(-k_i^j dt\right)\right]\left(V_i^{j,\infty} - V_i^j(t)\right) \tag{6}$$

$$k_i^j = A_0 \exp\left(-\frac{E_i^j}{RT(t)}\right); \quad V_i^{j,\infty} = V_{max}(j)\cdot m_0 \cdot f_j\left(E_i^j\right); \quad V_i^j(t=0) = 0 \tag{7}$$

Where N_p is the number of increment points in each distribution, k_i^j is the reaction rate constant for ith reaction in distribution j, E_i^j and $f_j\left(E_i^j\right)$ are corresponding activation energy and distribution value. The final form of the conversion rate $X_{cal}(t)$ at experimental points $a(t_a)$ can be expressed as:

$$X_{cal}(t) = 1 - \frac{1}{m_0}\sum_{t=0}^{t=t_a}\sum_{j=1}^{3}\sum_{i=1}^{N_p}\left[1 - exp\left(-k_i^j dt\right)\right]\left(V_i^{j,\infty} - V_i^j(t)\right) \tag{8}$$

Finally, kinetic parameters in the three distributions are identified by optimizing the objective function F, which is the residual sum of squares (RSS) between the experimental conversion rate $X_{exp}(t)$ and the calculated conversion rate $X_{cal}(t)$. Here, N_{exp} is the total number of experimental values:

$$F(parameters) = \sum_{a=1}^{N_{exp}}\sum_{t=0}^{t_a}\left(X_{\exp}(t) - X_{cal}(t)\right)^2 \tag{9}$$

The numerical discretization was combined with in-house MATLAB code, and the derivative-free Nelder–Mead simplex algorithm [49] was used to minimize the objective function. Herein, an entire set of data from two dynamic tests was used to compute the objective function. In order to avoid local minima, the initial set of parameters was derived from the solution values obtained in our previous study [42]. In addition, intentional perturbations were applied after identification to restart the procedure and check the stability

of the solution. To evaluate the discrepancy between experiments and model, two criteria, root mean square error (RMSE) and maximum deviation (D_m), were used:

$$RMSE = \frac{\sqrt{\sum_{a=1}^{N_{exp}} \sum_{t=0}^{t_a} \left(X_{exp}(t) - X_{cal}(t)\right)^2}}{N_{exp}} \quad (10)$$

$$D_m = Max\left|X_{exp}(t) - X_{cal}(t)\right|, \ \ \forall t \in [0, t_a] \quad (11)$$

3. Results and discussions

3.1 Thermogravimetric results

Figure 2 depicts the DRM curves of spruce and poplar at two different heating rates. Three distinct regions could be identified for both species. In the first temperature region, the DRM was stable from 100 °C to 200 °C. At this temperature, hemicelluloses melt into the liquid form [50], but the production of volatiles remained very limited. The second region, from 250 °C to 400 °C, exhibited the most important release of volatiles due to the decomposition of hemicelluloses and cellulose. Within this region, random fragmentation of glycosidic bonds in cellulose and hemicellulose generated volatiles with high oxygen contents and left carbonaceous residues [51]. Lignin pyrolysis and secondary charring of volatiles mainly corresponded to the last region, from 400°C to 800 °C, where the main charring process occurred in the form of re-organization of benzene rings into polycyclic structures [28].

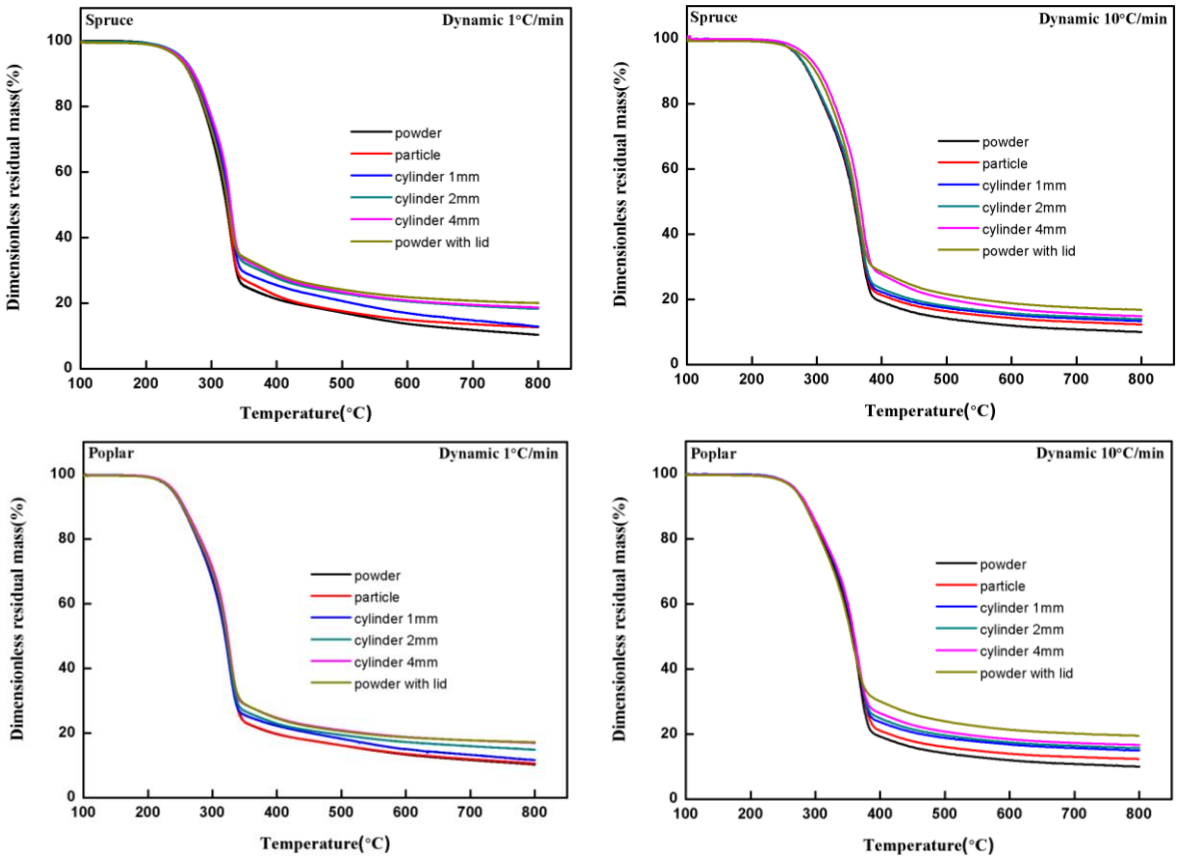

Figure 2. Pyrolysis DRM curves of spruce and poplar samples at two heating rates.

Mass transfer limitations occurring in large particles or in the crucible with lid promoted final char yields, and major differences emerged in the last temperature regions, which clearly indicated different pyrolysis mechanisms. These deviations began at around 330 °C at 1 °C/min and 370 °C at 10 °C/min for both spruce and poplar. The effect of particle sizes enlarged differences at high temperatures, where the mass loss was mainly associated with the rearrangement of residue in the charring process [52], including the important conversion of aromatic structures through demethoxylation [53], dehydration, cross-linking, and re-polymerization [27]. Specifically for the final DRM values (final char yields) of all particle types, the powder presented the lowest values due to the open microstructure and fast release of volatiles. Yet, accompanied by enlargement from powder to the 4 mm-cylinder, kinetic differences turned into noticeable char yield increases. Spruce had an increase in DRM from 10.3 wt.% to 18.7 wt.% at 1 ºC/min and from 10.0 wt.% to 14.8 wt.% at 10 ºC/min, and

poplar rose from 10.3 wt.% to 16.9 wt.% at 1 ºC/min and from 10.0 wt.% to 16.7 wt.% at 10 ºC/min. Therefore, setting the wood powder as a reference, the increase of particle size promoted char yields by 81% (1 ºC/min) and 48% (10 ºC/min) for spruce, and 65% (1 ºC/min) and 66% (10 ºC/min) for poplar. In contrast, the powder with a lid exhibited the maximum increase for all cases, confirming the occurrence of further charring reactions among the gaseous phase [54]. Obstruction of the mass transfer efficiency decisively promotes charring in the sample matrix [25], either by increasing the residence time or promoting secondary reactions within the solid matrix. Therefore, increased char formation by both intra- and extra-particle mass transfer limitations caused different thermogravimetric behaviors.

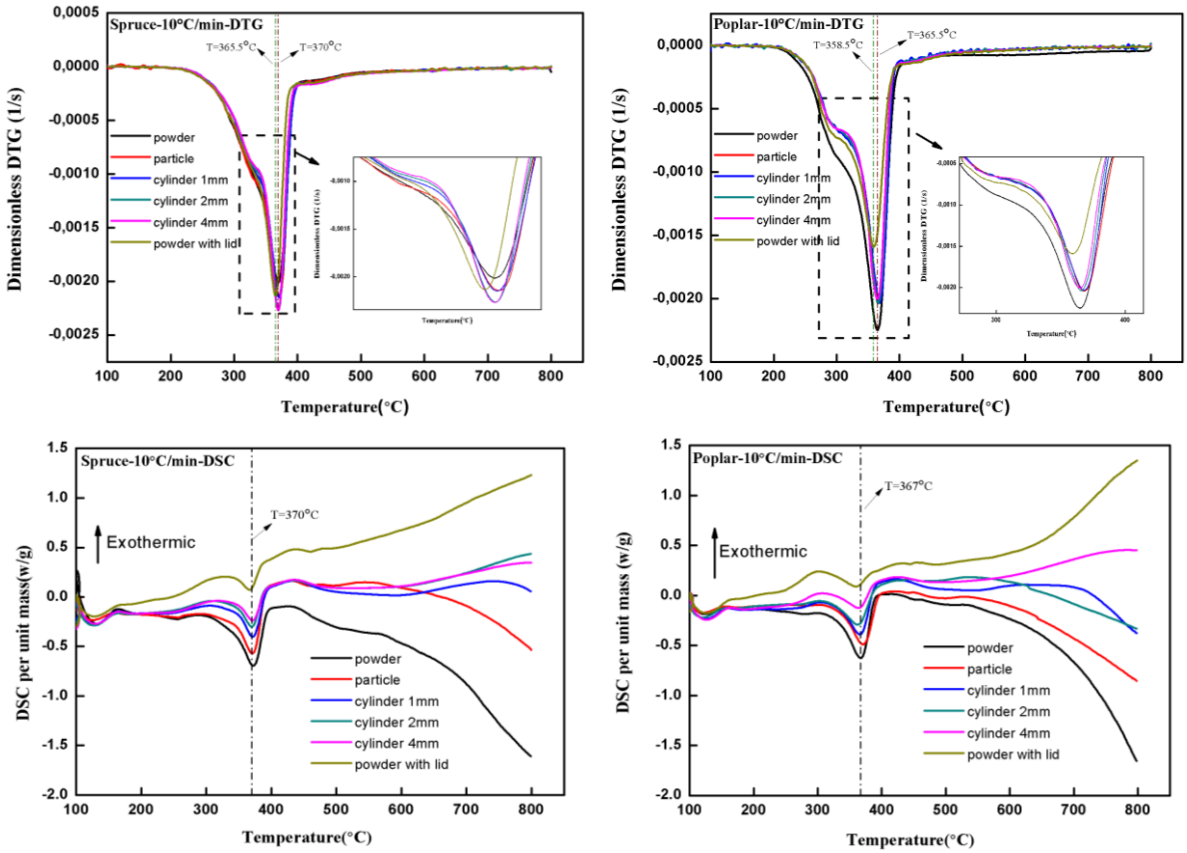

Figure 3. DTG (first row) and DSC (second row) signals normalized to the mass of spruce and poplar at 10°C/min.

In light of the shift of DSC baseline over long times and the fluctuation of derivative thermogravimetry (DTG) baseline for 1 °C/min tests, DSC and DTG curves at 10 °C/min

were selected here to further analyze the kinetic differences (Figure 3). The DTG and DSC signals were divided by the initial anhydrous mass of the samples. DTG curves exhibited similar trends between samples, but with noticeable differences between 300 °C and 400 °C in spruce, while more differences appeared between 270 °C and 415 °C in poplar. Major peaks appeared around the same temperatures: 370 ºC for spruce and 365.5 ºC for poplar, attributed to the rapid decomposition of cellulose. Curve shoulders at lower temperatures, 320–350 ºC, belonged to hemicellulose decomposition, which flattened and shifted towards higher temperatures at increasing particle sizes, indicating the delayed decomposition of hemicellulose. Meanwhile, the peak temperatures for the powder sample with lid shifted from 370 ºC to 365.5 ºC for spruce and from 365.5 ºC to 358.5 ºC for poplar, which is attributed to the condensation of highly reactive tarry volatiles inside the lidded crucibles [55].

The analysis of DSC data will be focused on the temperature range of 250–600 ºC. Since the signal was very small below this range and, as seen on the curves in Figure 3, the heat flux signal was seriously affected by radiation at higher temperatures [56]. From powder to cylinders, endothermic DSC peaks (around 370 ºC for spruce and 367 ºC for poplar) were in good accordance with the DTG peaks of cellulose decomposition. This major endothermicity corresponded to the depolymerization of the 1,4-glycosidic bond and ring breakage of light oxygenates [57]. The transition from endothermic to exothermic in large particles was possibly caused by cellulosic char formation due to the presence of alkyl furans, benzenoid aromatics, and condensed aromatics [58, 59]. An obvious tendency of heat release was observed as the particle size increased for both wood species. This important exothermicity was assigned to carbonization including re-polymerization and cross-linking in aromatic residues [60], in which exothermic heat had been proven to be proportional to char yield [61]. The alteration of thermal profile therefore indicated the enhancement of exothermic charring in large particles. In contrast, for the powder sample with lid, its largest exothermicity was

attributed to the hindered volatile escape that enhanced condensation and charring [62]. Detained volatiles went through severe secondary carbonizations both homogeneously and heterogeneously, evidenced by the experimental observations of carbon depositions on the inner walls of the crucible, and the lid.

The O/C and H/C ratios of residual char were indicators for carbonization degree [63], they were therefore coupled with the dimensionless mass loss (DML) of different particle sizes for analysis purposes (full set of data can be found in the supporting material, Supplementary Table 1). For both wood species at both heating rates, DML decreased consistently due to secondary charring. Meanwhile, the decreasing trends of H/C and O/C ratios indicated that char became more carbonaceous [64] because of dehydration and demethylation. Dehydration drove the oxidation of saturated hydrocarbons to form aromatic structures, serving as the precursor for biochar [65]. And the methyl removal in demethylation decreased the H/C ratio for C enrichment in the char product [66].

Static tests of two wood types at six temperature levels were conducted in advance, (detailed data of atomic ratios vs. DML can be found in the supporting material, Supplementary Table 2). Then, dynamic tests at 10 °C/min, were chosen as reference and further compared in Figure 4. Two opposite relations were identified: dynamic tests had increasing DML values that matched with decreasing carbonization degree (increases in O/C and H/C), while static tests showed the opposite relation between DML and carbonization. Small size and low temperature (<500 °C) dominantly triggered the decompositions of non-aromatic carbon bonds in lignin [67], causing the changes in the DML. However, different thermochemical pathways in the dynamic tests indicated interceptions of primary volatiles that interacted with recondensation products, contributing directly to decreased DML in large particles. And the simultaneous polymerization and secondary charring reactions caused higher degrees of carbonization. Therefore, abovementioned two converse matching

relationship between DML and carbonization clearly indicated the traces of enhanced charring while increasing particle sizes.

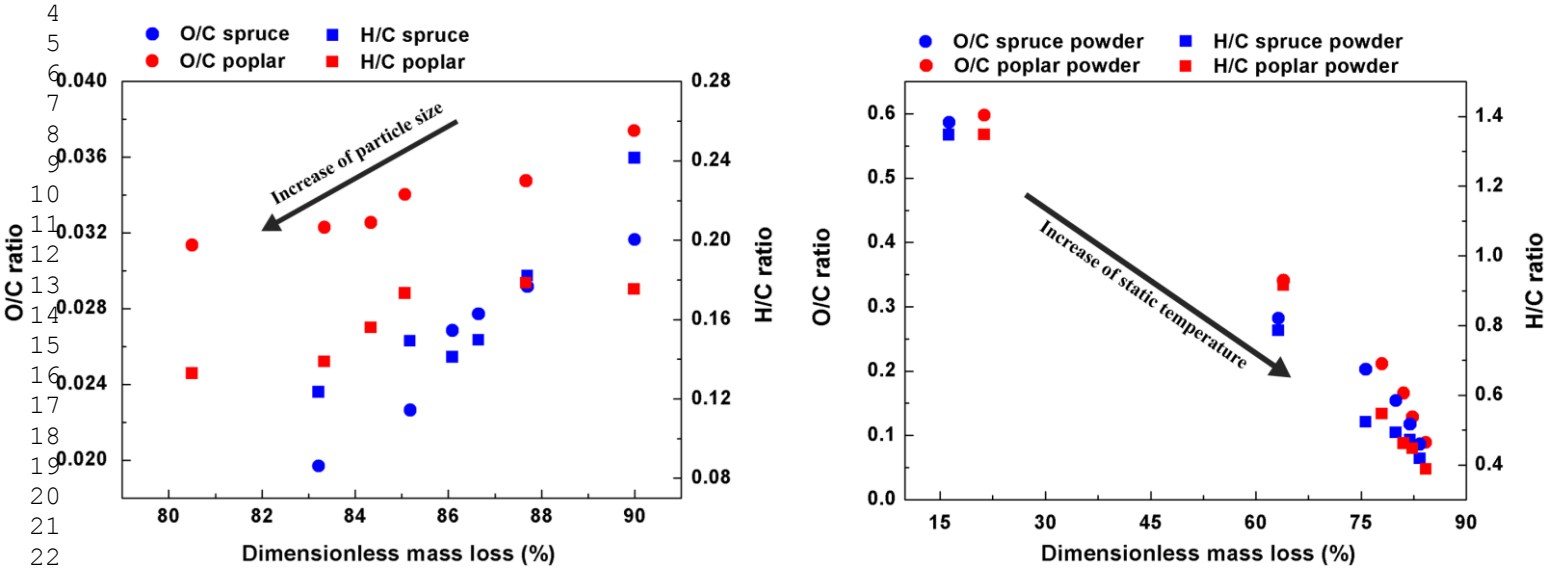

Figure 4. Atomic O/C, H/C ratios vs. DML in dynamic tests with different particle sizes of spruce and poplar (left); in static tests of spruce and poplar powder (right)

3.2 DAEM modeling

3.2.1 Model identification

Kinetic parameters fitted to the two Gaussian distributions and one exponential distribution in DAEM are listed in Table 2 for all samples. The corresponding full sets of experimental and simulated DRM curves could be found in the supporting material (Supplementary Figure 2). The root mean square error (RMSE) and maximum deviation (D_m) for each particle condition assessed the quality of identification. The reasonably low ranges of RMSE values: 0.98×10^{-4} –1.64×10^{-4} for spruce and 0.47×10^{-4} –0.84×10^{-4} for poplar indicated very small deviations in general, which confirmed the relevancies of number and shapes of the distributions [68]. Furthermore, the maximum deviation D_m presented in acceptable ranges: 2.77% –4.08% for spruce and 1.87% –3.34% for poplar. Usually, this error was not visually obvious in the curves because it tended to appear in fast decomposition regions (250 °C to 350 °C), where the curve slopes were very large. Therefore, these two indexes

exhibited reasonably small deviations and ensured simulation accuracies. While the identified model parameters had ensured correct overlaps between the simulated and experimental curves, they can also capture the detailed kinetic differences thanks to the "point-by-point" fitting nature during identification process.

General characteristics of three distributions' parameters were consistent with previous work [35, 69], namely the lowest content of the first Gaussian, the largest content and narrowest range of the second Gaussian, and the exponential exhibited partial overlap with the other two distributions. Herein, $V_{max}1$, the weighting factor of the first distribution, generally decreased when particle size increased from powder to 4-mm cylinder for both wood species, indicating that secondary charring undermined the volatile contributions of the first pseudo-component (hemicellulose) in large particles. $V_{max}1$ was less affected for powder with lid, which was possibly due to the heterogeneous gaseous reactions outside particles that led to devolatilization [70]. The other two weighting factors followed complicated variation trends that will be further investigated in the subsequent section. Nonetheless, the comprehensive parameters of various particle sizes served as good resources for other kinetic researches.

An advantage of the robust DAEM model was that devolatilization in the three pseudo-components can be analyzed independently. The inverse reconstructions of devolatilization profiles of pseudo-components allows the effect of particle size to be further analyzed. This merit was exemplified by the devolatilization profiles of three extreme sample sizes (powder, 4-mm cylinder, and powder with lid), and detailed comparisons were also presented in supporting material.

Table 2. Identified two Gaussian + one exponential DAEM parameters for different particle sizes of spruce and poplar

Biomass	Spruce						Poplar					
Size condition	Powder	Particle	Cylinder 1 mm	Cylinder 2 mm	Cylinder 4 mm	Powder with lid	Powder	Particle	Cylinder 1 mm	Cylinder 2 mm	Cylinder 4 mm	Powder with lid
$V_{max}1$	0.1670	0.1130	0.1115	0.1140	0.1070	0.1520	0.1704	0.1402	0.1316	0.1183	0.0951	0.1620
$V_{max}2$	0.4704	0.4683	0.4801	0.4248	0.4149	0.3643	0.4902	0.5258	0.5136	0.4960	0.4622	0.4179
$V_{max}3$	0.2913	0.3168	0.3129	0.2540	0.2862	0.2866	0.2556	0.2461	0.2713	0.2452	0.2777	0.2496
A_0(s^{-1})	8.19×10^{15}	3.60×10^{16}	1.55×10^{14}	1.90×10^{15}	1.07×10^{15}	4.66×10^{14}	1.94×10^{13}	3.75×10^{12}	1.03×10^{12}	8.03×10^{12}	7.30×10^{13}	8.24×10^{13}
E_0_1(kJ/mol)	201.30	209.56	182.40	191.18	187.12	184.69	169.05	160.52	154.10	163.75	174.11	171.86
E_0_2(kJ/mol)	216.58	224.08	197.38	209.95	206.80	201.21	186.39	178.31	171.15	181.73	192.72	193.10
E_{min}(kJ/mol)	176.10	185.94	160.88	188.35	184.00	180.32	150.29	143.99	137.76	148.15	158.54	169.37
σ_1 (kJ/mol)	3.86	2.12	1.20	10.23	12.53	12.55	4.43	2.75	1.47	1.84	1.34	7.51
σ_2 (kJ/mol)	9.82×10^{-7}	7.21×10^{-3}	5.93×10^{-8}	7.37×10^{-7}	1.27×10^{-6}	4.98×10^{-6}	2.84×10^{-7}	2.83×10^{-6}	4.79×10^{-7}	1.61×10^{-7}	2.45×10^{-7}	5.76×10^{-9}
β	0.49	0.31	0.56	0.27	0.26	0.24	0.51	0.51	0.63	0.40	0.32	0.26
RMSE ($\times10^{-4}$)	1.11	0.98	1.07	1.64	1.58	1.34	0.84	0.47	0.60	0.48	0.58	0.81
D_m(%)	3.46	4.08	2.92	3.78	3.74	2.77	3.34	1.87	2.26	2.12	2.22	2.79

Since kinetic parameters in each group interacted with dependences, their direct analysis might suffer from complicated interactions that led to non-specific effects of particle size. Instead, synthetic indexes were therefore built: $T_p(j)$ and $V_p(j)$, $j\epsilon[1:3]$ were the temperature and dimensionless volatile quantities corresponding to the maximum devolatilization rate for the three pseudo-components (Table 3).

$$V_p(j) = Max\left|\left[1 - exp\left(-k_i^j dt\right)\right]\left(V_i^{j,\infty} - V_i^j(t)\right)\right|, \forall i \in [1, N_p] \quad (12)$$

$T_p(1)$ generally decreased in spruce when particle size increased but was stable in poplar, possibly due to their different hemicellulose structures. Namely, monosaccharide units in spruce which are more easily decomposed [71, 72] than the glucomannan units in poplar. The decreasing trend of $V_p(1)$ for both species indicated that the first pseudo-component reduced its devolatilization contributions in large particles. $T_p(2)$ underwent limited changes while particle size increased in both species. This can be explained by the cellulose crystalline structure that decomposed rapidly once reaching the melting point [73]. This stable temperature-dependence indicated that the $T_p(2)$ value was more related to chemical alteration than to particle size [74]. Furthermore, the devolatilization amount of spruce second pseudo-component was more affected by the particle size, as revealed by more decrease trend of $V_p(2)$ in spruce compared to that in poplar. A general increase of $T_p(3)$ in spruce indicated that the decomposition of the third pseudo-component was shifted towards higher temperatures in large particles, which was possibly caused by the increase of activation energy during charring reactions [75].

Table 3. Synthetic values of three pseudo-components in spruce and poplar in dynamic tests at 10°C/min.

Pseudo-component	Peak values	Spruce						Poplar					
		Powder	Particle	Cylinder, 1mm	Cylinder, 2mm	Cylinder, 4mm	Powder With lid	Powder	Particle	Cylinder, 1mm	Cylinder, 2mm	Cylinder, 4mm	Powder with lid
First	Tp(1)	283.75	288.94	282.94	270.74	265.84	269.34	267.45	264.74	263.33	265.33	268.05	254.84
	Vp(1)	3.85	3.14	2.68	1.79	1.22	1.54	3.26	3.08	3.12	2.87	2.51	2.37
Second	Tp(2)	327.65	328.34	328.06	329.04	328.14	323.55	325.24	324.93	321.84	324.14	325.05	324.35
	Vp(2)	12.77	12.81	12.42	11.38	10.98	9.54	11.86	12.21	11.59	11.76	11.56	10.49
Third	Tp(3)	234.46	242.55	238.36	284.54	279.54	279.63	231.24	232.34	229.95	234.84	237.74	269.55
	Vp(3)	1.13	1.85	1.06	1.56	1.84	1.99	0.96	0.91	0.83	1.12	1.57	1.59

*$T_p(j)$: Peak temperature, °C.

$V_p(j)$: Dimensionless volatile, 10^{-4}.

j: Pseudo-component, $j\epsilon[1:3]$.

3.2.2 Model validation

Prediction of mass loss

The model parameters commented previously were identified from the learning database, which consisted of dynamic tests performed at 1 and 10 °C/min. To further assess model's prediction potential, these identified parameters were subsequently used to simulate static tests (Figure 5). The final DRM (Dimensionless Residual Mass) values (DRM = 1-DML) were calculated for all samples. Three temperature levels (300, 500, and 800 °C) were chosen to represent three typical pyrolytic stages: initial decomposition, major pyrolysis, and secondary reaction [1, 76].

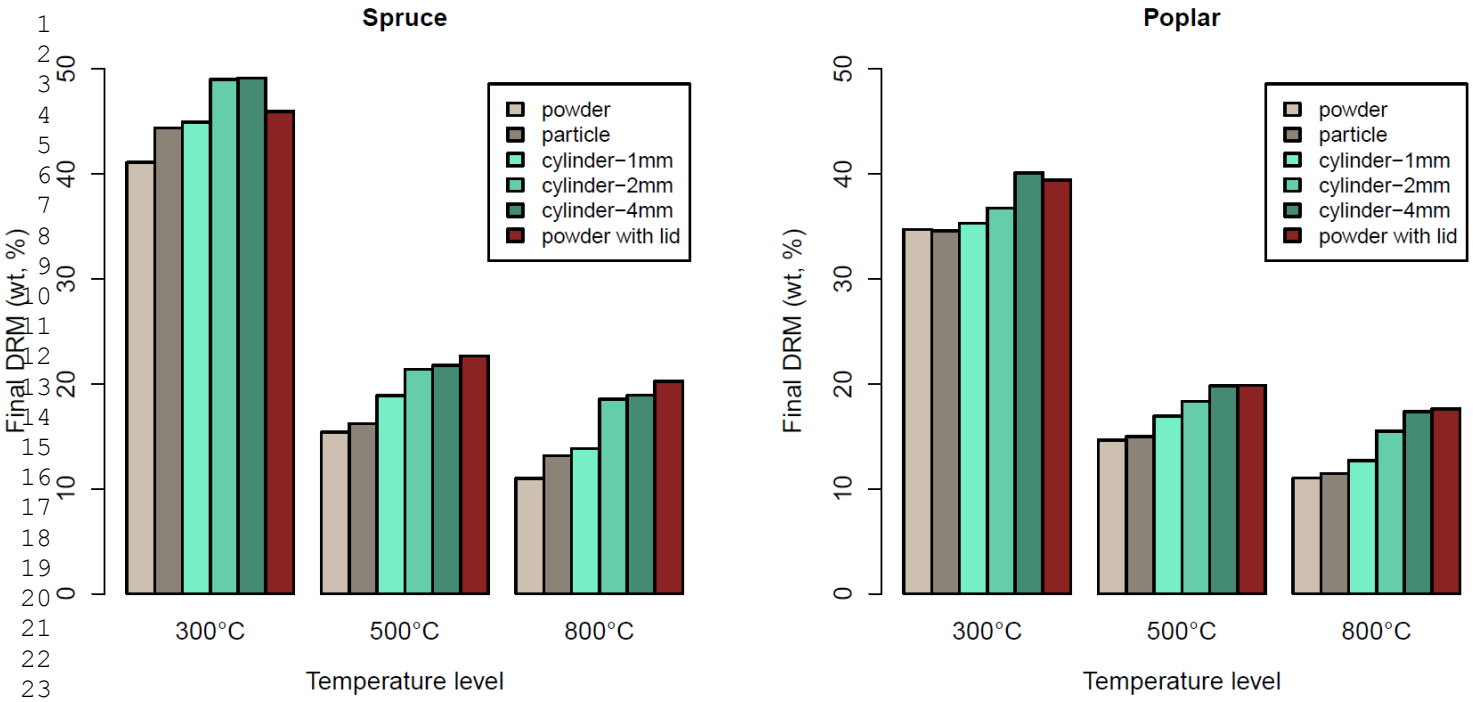

Figure 5. Predictions of final DRM values of spruce and poplar samples in three static tests performed at different temperature levels (300, 500, and 800 °C)

For both spruce and poplar, the predicted DRM values at all chosen temperature levels simultaneously increased when increasing the particle size from powder to the 4-mm cylinder. As direct effect of particle size, the promotion of char formation by intra-particle mass transfer limitations is well-admitted [25] and included in the learning database, proving the logical and reasonable features of numerical predictions. Regarding the effect of temperature level, it was understandable that further devolatilization caused generally lower DRM values at 500 °C compared to those at 300 °C, and the final high-temperature decomposition of lignin and partial secondary cracking reactions caused the lowest DRM values at 800 °C. Meanwhile, the powder with lid exhibited the largest char yield at 500 and 800 °C levels for both species, corresponding to the experimental findings of the most severe char depositions inside the lidded crucibles. Note however that the DRM of powder with lid found at 300°C is smaller than the two longer cylinders.

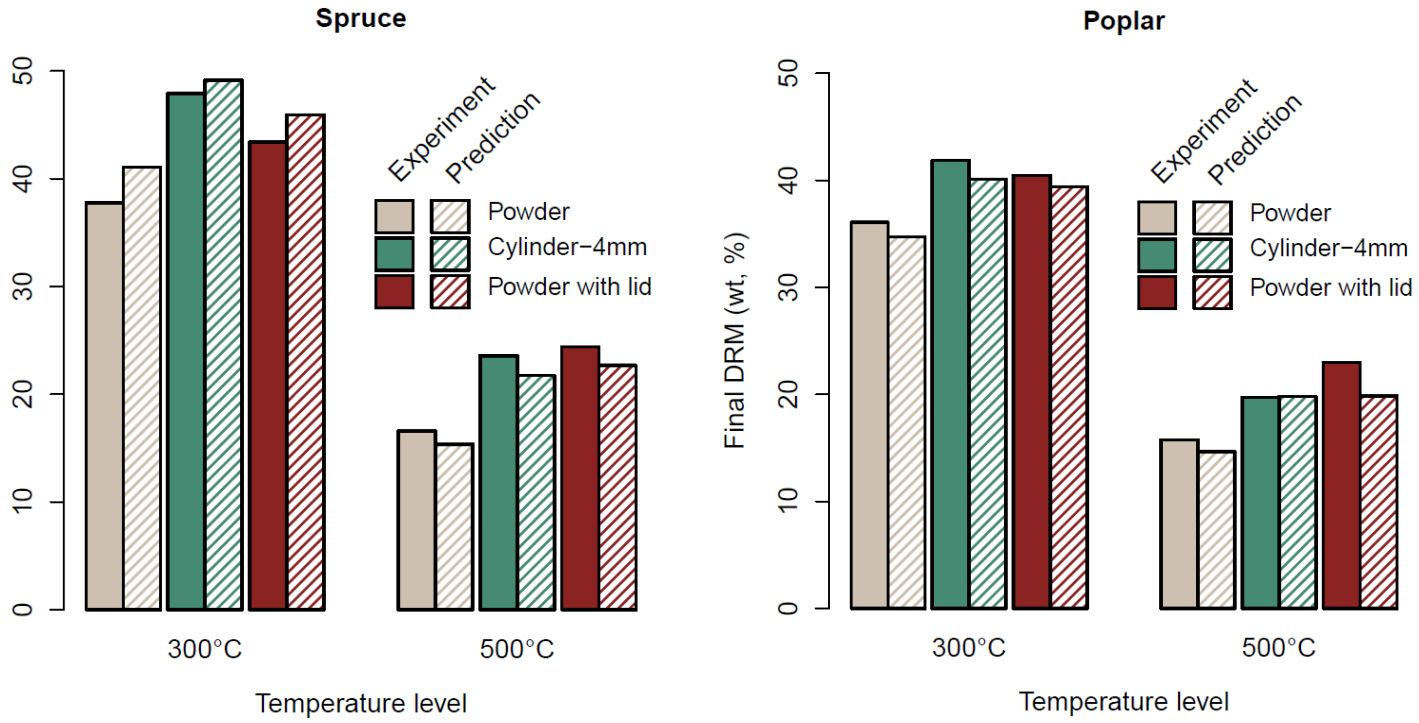

436 Figure 6. Experiment validations of residual mass for powder, 4mm cylinder and powder with
437 lid for static tests at 300°C, 500 °C for spruce and poplar

438 Static tests at 300 °C and 500 °C were performed for the purpose of validation (Figure
439 6). Herein, the static test at 300 °C was a particularly demanding validation case because the
440 kinetics was very slow at this temperature, resulting in very partial volatilization at the end of
441 the experiment, likely to introduce prediction errors. In this research, due to the strict
442 sampling protocol that largely limited the sample amount, only representative sample types
443 (powder, 4-mm cylinder, powder with lid) were tested. The comparison between experiment
444 and prediction depicted excellent trends with limited errors for all conditions. The error
445 ranges, 1.20–3.31% for spruce and 1.09–3.12% for poplar, were more acceptable compared to
446 previously published works proposing predictions [77]. And it was remarkable to observe that
447 the smaller DRM value of powder with lid predicted at 300 °C was confirmed by the
448 experiment.

To conclude, kinetic differences originated from intra-particle limitations were nicely predicted by the model, despite the very different time–temperature pathways between validation database and learning database. And this section demonstrated model's prediction ability on the volatilizations for contrasted pyrolysis conditions.

Prediction of char composition

As commented in the experimental section, the relation between char composition and DML revealed the presence of secondary charring when changing particle size. Assuming that the extra char produced from secondary charring has the identical elemental compositions, i.e., not affected by the particle size. Accordingly, the elemental composition can be deduced as a weighted average value of primary reactions and secondary charring (eq.13). Herein, wood powder is used as the reference for primary reactions.

This weighted average allows the element contents of char (c_1 to c_4) to be predicted from the elemental contents of powder and secondary charring, the DRM of powder and the change of DRM with the considered particle:

$$c_i = \frac{\left(DRM_{powder}\right) \cdot \alpha_i + \Delta DRM \cdot \beta_i}{DRM_{powder} + \Delta DRM}, \quad i \in [1{:}\,4] \tag{13}$$

Where DRM_{powder} is the dimensionless residual mass of wood powder, ΔDRM the additional residual mass of the particle compared to powder, α_i the contents in the char of wood powder, and β_i, the element contents in char produced by secondary charring. Indices *i* stands for carbon, hydrogen, oxygen, and ash. It is assumed that char from secondary charring contains no ash:

$$\beta_C + \beta_H + \beta_O = 1; \qquad \beta_{ash} = 0 \tag{14}$$

An identification process was conducted for minimizing the RMSE between c_i and actual experimental values at 10 °C/min, to obtain β_i for both wood species (Table 4). To be

noted, the highly dominant content of carbon (β_C) confirms that carbonization is the major effect of secondary reactions.

Table 4. Identified element content parameters in two wood species at 10 °C/min

Wood Species	β_C	β_H	β_O
Spruce	0.9885	4.4712×10^{-10}	0.01149
Poplar	0.9582	9.1484×10^{-3}	0.03265

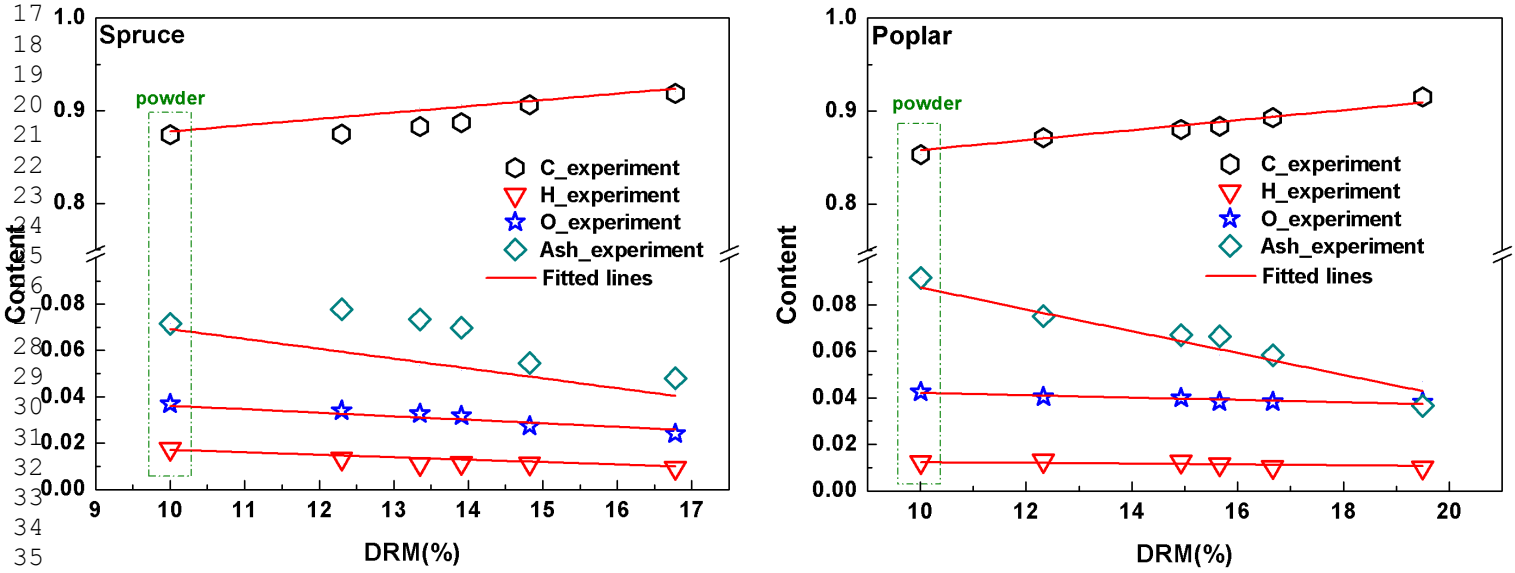

Figure 7. Elementary contents *vs*. dimensionless residual mass (DRM) of samples with different particle sizes in the 10 °C/min dynamic tests, and corresponding fitted curves

The predictions using equation (13) together with the composition of secondary charring (Table 4) were plotted for both species (Figure 7), which depicts an excellent correlation between the change of composition and the change of DRM. The good correlation obtained for ash is consistent with the assumption on the absence of ash in secondary reactions. In practice, this observation allows a clear conclusion to be drawn. As the kinetic prediction of the DAEM model is already validated, the change of DRM between a certain particle size and powder can be predicted for any time-temperature profile. Hence, equation (8) supplied with

the data of table 4, can be used to predict the elemental analysis of char whatever the conditions underwent by the particle. To that purpose, the elemental analysis of char from powder could be predicted as a function of the Dimensionless Residual Mass (DRM) thanks to the correlation proposed in [42]:

$$\frac{O}{C} = 1.134 - 0.219 \times \exp(1.815 - 1.815DRM)$$
$$\frac{H}{C} = 0.1534 - 0.0268 \times \exp(1.783 - 1.783DRM) \quad (15)$$

This opens new possibilities in process design and control, as this method can be applied to any industrial process, as long as the conditions imposed to the particles were provided. This could be applied, for example, to the prediction of elemental composition along the reactor height for the pyrolysis of a packed bed [34].

4. Conclusions

This study is devoted to the effect of particle size on the pyrolysis of two wood species: spruce and poplar. Various sample geometries treated in TG/DSC allowed comprehensive analyses of the mass and heat limitations from intra-particle (powder to cylinder) and reactor type (crucible with and without lid). A negative mass loss/carbonization pathway confirmed additional charring at increasing particle size. Exothermicity from char formation was promoted by particle size (or extra-particle limitations).

From this learning database, a robust DAEM model, with two Gaussian and one exponential DAEM distributions, was derived. The DAEM model was used to simulate and predict mass loss for different time-temperature profiles. These predictions were successfully validated by additional experiments. The composition of char produced by secondary charring was determined from the linear relation found between elemental analyses and residual mass. This allows the elemental composition of char to be predicted for a given

particle size for any time-temperature pathway. This prediction involves the kinetic differences between powder and a given particle, as predicted by the DAEM model.

In conclusion, this paper addresses the important question of the effect of particle size on biomass pyrolysis and proposes simulation tools to predict the kinetics and the elemental composition of char. These tools are intended for use in the design and control of industrial processes.

Acknowledgements

The authors are grateful for the financial support of the Conseil Général de la Marne, Grand Reims and the Région Grand Est, France. The support from the China Scholarship Council (CSC) is also gratefully acknowledged.

References

[1] A. Demirbas, G. Arin, An overview of biomass pyrolysis, Energy sources 24(5) (2002) 471-482.
[2] M.N. Uddin, W.W. Daud, H.F. Abbas, Effects of pyrolysis parameters on hydrogen formations from biomass: a review, Rsc Advances 4(21) (2014) 10467-10490.
[3] T. Kan, V. Strezov, T.J. Evans, Lignocellulosic biomass pyrolysis: A review of product properties and effects of pyrolysis parameters, Renewable and Sustainable Energy Reviews 57 (2016) 1126-1140.
[4] D. Chen, Y. Li, K. Cen, M. Luo, H. Li, B. Lu, Pyrolysis polygeneration of poplar wood: Effect of heating rate and pyrolysis temperature, Bioresource Technology 218 (2016) 780-788.
[5] R. Kumar, V. Strezov, H. Weldekidan, J. He, S. Singh, T. Kan, B. Dastjerdi, Lignocellulose biomass pyrolysis for bio-oil production: A review of biomass pre-treatment methods for production of drop-in fuels, Renewable and Sustainable Energy Reviews 123 (2020) 109763.
[6] K. Kirtania, S. Bhattacharya, Coupling of a distributed activation energy model with particle simulation for entrained flow pyrolysis of biomass, Fuel processing technology 137 (2015) 131-138.
[7] C. Di Blasi, Modeling intra- and extra- particle processes of wood fast pyrolysis, AIChE journal 48(10) (2002) 2386-2397.
[8] P.O. Okekunle, H. Watanabe, T. Pattanotai, K. Okazaki, Effect of biomass size and aspect ratio on intra-particle tar decomposition during wood cylinder pyrolysis, Journal of Thermal Science and Technology 7(1) (2012) 1-15.

[9] P. Perre, R. Remond, I. Turner, A comprehensive dual-scale wood torrefaction model: Application to the analysis of thermal run-away in industrial heat treatment processes, International Journal of Heat and Mass Transfer 64 (2013) 838-849.
[10] I. Turner, P. Rousset, R. Rémond, P. Perré, An experimental and theoretical investigation of the thermal treatment of wood (Fagus sylvatica L.) in the range 200–260 C, International Journal of Heat and Mass Transfer 53(4) (2010) 715-725.
[11] A. Bharadwaj, L.L. Baxter, A.L. Robinson, Effects of intraparticle heat and mass transfer on biomass devolatilization: experimental results and model predictions, Energy & fuels 18(4) (2004) 1021-1031.
[12] D.V. Suriapparao, R. Vinu, Effects of biomass particle size on slow pyrolysis kinetics and fast pyrolysis product distribution, Waste and biomass valorization 9(3) (2018) 465-477.
[13] H. Haykiri-Acma, The role of particle size in the non-isothermal pyrolysis of hazelnut shell, Journal of analytical and applied pyrolysis 75(2) (2006) 211-216.
[14] J. Herguido, J. Corella, J. Gonzalez-Saiz, Steam gasification of lignocellulosic residues in a fluidized bed at a small pilot scale. Effect of the type of feedstock, Industrial & engineering chemistry research 31(5) (1992) 1274-1282.
[15] O. Beaumont, Y. Schwob, Influence of physical and chemical parameters on wood pyrolysis, Industrial & Engineering Chemistry Process Design and Development 23(4) (1984) 637-641.
[16] J. Shen, X.-S. Wang, M. Garcia-Perez, D. Mourant, M.J. Rhodes, C.-Z. Li, Effects of particle size on the fast pyrolysis of oil mallee woody biomass, Fuel 88(10) (2009) 1810-1817.
[17] A. Demirbas, Effects of temperature and particle size on bio-char yield from pyrolysis of agricultural residues, Journal of analytical and applied pyrolysis 72(2) (2004) 243-248.
[18] S. Zhou, M. Garcia-Perez, B. Pecha, A.G. McDonald, R.J. Westerhof, Effect of particle size on the composition of lignin derived oligomers obtained by fast pyrolysis of beech wood, Fuel 125 (2014) 15-19.
[19] R.J.M. Westerhof, H. Nygard, W.P.M. van Swaaij, S.R. Kersten, D.W.F. Brilman, Effect of particle geometry and microstructure on fast pyrolysis of beech wood, Energy & fuels 26(4) (2012) 2274-2280.
[20] T.J. Haas, M.R. Nimlos, B.S. Donohoe, Real-time and post-reaction microscopic structural analysis of biomass undergoing pyrolysis, Energy & Fuels 23(7) (2009) 3810-3817.
[21] C. Brackmann, M. Aldén, P.-E. Bengtsson, K.O. Davidsson, J.B. Pettersson, Optical and mass spectrometric study of the pyrolysis gas of wood particles, Applied spectroscopy 57(2) (2003) 216-222.
[22] R.J.M. Westerhof, Refining fast pyrolysis of biomass, (2011).
[23] O. Boutin, M. Ferrer, J. Lédé, Flash pyrolysis of cellulose pellets submitted to a concentrated radiation: experiments and modelling, Chemical Engineering Science 57(1) (2002) 15-25.

[24] M.J. Antal, E. Croiset, X. Dai, C. DeAlmeida, W.S.-L. Mok, N. Norberg, J.-R. Richard, M. Al Majthoub, High-yield biomass charcoal, Energy & Fuels 10(3) (1996) 652-658.
[25] A. Anca-Couce, R. Mehrabian, R. Scharler, I. Obernberger, Kinetic scheme of biomass pyrolysis considering secondary charring reactions, Energy Conversion and Management 87 (2014) 687-696.
[26] F. Richter, A. Atreya, P. Kotsovinos, G. Rein, The effect of chemical composition on the charring of wood across scales, Proceedings of the Combustion Institute 37(3) (2019) 4053-4061.
[27] C.A. Zaror, I.S. Hutchings, D.L. Pyle, H.N. Stiles, R. Kandiyoti, Secondary char formation in the catalytic pyrolysis of biomass, Fuel 64(7) (1985) 990-994.
[28] F.-X. Collard, J. Blin, A review on pyrolysis of biomass constituents: Mechanisms and composition of the products obtained from the conversion of cellulose, hemicelluloses and lignin, Renewable and Sustainable Energy Reviews 38 (2014) 594-608.
[29] D.F. Arseneau, Competitive reactions in the thermal decomposition of cellulose, Canadian Journal of Chemistry 49(4) (1971) 632-638.
[30] S.R. Kersten, X. Wang, W. Prins, W.P. van Swaaij, Biomass pyrolysis in a fluidized bed reactor. Part 1: Literature review and model simulations, Industrial & engineering chemistry research 44(23) (2005) 8773-8785.
[31] V. Vand, A theory of the irreversible electrical resistance changes of metallic films evaporated in vacuum, Proceedings of the Physical Society 55(3) (1943) 222.
[32] J. Zhang, T. Chen, J. Wu, J. Wu, Multi-Gaussian-DAEM-reaction model for thermal decompositions of cellulose, hemicellulose and lignin: Comparison of N2 and CO2 atmosphere, Bioresource technology 166 (2014) 87-95.
[33] C.N. Arenas, M.V. Navarro, J.D. Martínez, Pyrolysis kinetics of biomass wastes using isoconversional methods and the distributed activation energy model, Bioresource technology 288 (2019) 121485.
[34] S. Cavagnol, J.F. Roesler, E. Sanz, W. Nastoll, P. Lu, P. Perré, Exothermicity in wood torrefaction and its impact on product mass yields: From micro to pilot scale, The Canadian Journal of Chemical Engineering 93(2) (2015) 331-339.
[35] J. Cai, W. Wu, R. Liu, An overview of distributed activation energy model and its application in the pyrolysis of lignocellulosic biomass, Renewable and Sustainable Energy Reviews 36 (2014) 236-246.
[36] T. Chen, J. Zhang, J. Wu, Kinetic and energy production analysis of pyrolysis of lignocellulosic biomass using a three-parallel Gaussian reaction model, Bioresource Technology 211 (2016) 502-508.
[37] C. Wang, L. Li, Z. Zeng, X. Xu, X. Ma, R. Chen, C. Su, Catalytic performance of potassium in lignocellulosic biomass pyrolysis based on an optimized three-parallel distributed activation energy model, Bioresource technology 281 (2019) 412-420.

[38] Z. Cheng, W. Wu, P. Ji, X. Zhou, R. Liu, J. Cai, Applicability of Fraser–Suzuki function in kinetic analysis of DAEM processes and lignocellulosic biomass pyrolysis processes, Journal of Thermal Analysis and Calorimetry 119(2) (2015) 1429-1438.
[39] J. Cai, W. Wu, R. Liu, G.W. Huber, A distributed activation energy model for the pyrolysis of lignocellulosic biomass, Green Chemistry 15(5) (2013) 1331-1340.
[40] J. Zhang, T. Chen, J. Wu, J. Wu, A novel Gaussian-DAEM-reaction model for the pyrolysis of cellulose, hemicellulose and lignin, Rsc Advances 4(34) (2014) 17513-17520.
[41] C. Couhert, J.-M. Commandre, S. Salvador, Is it possible to predict gas yields of any biomass after rapid pyrolysis at high temperature from its composition in cellulose, hemicellulose and lignin?, Fuel 88(3) (2009) 408-417.
[42] P. Perré, Y. Tian, P. Lu, B. Malinowska, J. El Bekri, J. Colin, A robust and frugal model of biomass pyrolysis in the range 100–800° C: Inverse analysis of DAEM parameters, validation on static tests and determination of heats of reaction, Fuel (2020) 119692.
[43] Y. Tian, P. Perré, Multiple-distribution DAEM modelling of spruce pyrolysis: An investigation of the best trade-off regarding the number and shape of distributions, Energy Conversion and Management 229 113756.
[44] M.S. Ahmad, H. Liu, H. Alhumade, M.H. Tahir, G. Çakman, A. Yıldız, S. Ceylan, A. Elkamel, B. Shen, A modified DAEM: To study the bioenergy potential of invasive Staghorn Sumac through pyrolysis, ANN, TGA, kinetic modeling, FTIR and GC–MS analysis, Energy Conversion and Management 221 (2020) 113173.
[45] G. Pitt, The kinetic of the evolution of volatile products from coal, Fuel 41 (1962) 267-274.
[46] C. Lakshmanan, M. Bennett, N. White, Implications of multiplicity in kinetic parameters to petroleum exploration: Distributed activation energy models, Energy & Fuels 5(1) (1991) 110-117.
[47] P. Perré, I.W. Turner, A 3-D version of TransPore: a comprehensive heat and mass transfer computational model for simulating the drying of porous media, International Journal of heat and mass transfer 42(24) (1999) 4501-4521.
[48] R. Remond, I. Turner, P. Perre, Modeling the drying and heat treatment of lignocellulosic biomass: 2D effects due to the product anisotropy, Drying Technology 28(8) (2010) 1013-1022.
[49] J.A. Nelder, R. Mead, A simplex method for function minimization, The computer journal 7(4) (1965) 308-313.
[50] T. Hosoya, H. Kawamoto, S. Saka, Cellulose–hemicellulose and cellulose–lignin interactions in wood pyrolysis at gasification temperature, Journal of analytical and applied pyrolysis 80(1) (2007) 118-125.
[51] M.B. Pecha, J.I.M. Arbelaez, M. Garcia-Perez, F. Chejne, P.N. Ciesielski, Progress in understanding the four dominant intra-particle phenomena of lignocellulose pyrolysis: chemical reactions, heat transfer, mass transfer, and phase change, Green chemistry 21(11) (2019) 2868-2898.

[52] Y. Peng, S. Wu, The structural and thermal characteristics of wheat straw hemicellulose, Journal of Analytical and Applied Pyrolysis 88(2) (2010) 134-139.
[53] Y. Le Brech, J. Raya, L. Delmotte, N. Brosse, R. Gadiou, A. Dufour, Characterization of biomass char formation investigated by advanced solid state NMR, Carbon 108 (2016) 165-177.
[54] W.S.L. Mok, M.J. Antal Jr, P. Szabo, G. Varhegyi, B. Zelei, Formation of charcoal from biomass in a sealed reactor, Industrial & engineering chemistry research 31(4) (1992) 1162-1166.
[55] L. Basile, A. Tugnoli, C. Stramigioli, V. Cozzani, Influence of pressure on the heat of biomass pyrolysis, Fuel 137 (2014) 277-284.
[56] M. Wolfinger, J. Rath, G. Krammer, F. Barontini, V. Cozzani, Influence of the emissivity of the sample on differential scanning calorimetry measurements, Thermochimica acta 372(1-2) (2001) 11-18.
[57] D.O. Usino, P. Ylitervo, A. Pettersson, T. Richards, Influence of temperature and time on initial pyrolysis of cellulose and xylan, Journal of Analytical and Applied Pyrolysis (2020) 104782.
[58] I. Pastorova, R.E. Botto, P.W. Arisz, J.J. Boon, Cellulose char structure: a combined analytical Py-GC-MS, FTIR, and NMR study, Carbohydrate research 262(1) (1994) 27-47.
[59] M.J. Antal, M. Grønli, The art, science, and technology of charcoal production, Industrial & Engineering Chemistry Research 42(8) (2003) 1619-1640.
[60] B. Shrestha, Y. Le Brech, T. Ghislain, S. Leclerc, V. Carré, F. Aubriet, S. Hoppe, P. Marchal, S. Pontvianne, N. Brosse, A multitechnique characterization of lignin softening and pyrolysis, ACS Sustainable Chemistry & Engineering 5(8) (2017) 6940-6949.
[61] L. Basile, A. Tugnoli, C. Stramigioli, V. Cozzani, Thermal effects during biomass pyrolysis, Thermochimica Acta 636 (2016) 63-70.
[62] Q. Chen, R. Yang, B. Zhao, Y. Li, S. Wang, H. Wu, Y. Zhuo, C. Chen, Investigation of heat of biomass pyrolysis and secondary reactions by simultaneous thermogravimetry and differential scanning calorimetry, Fuel 134 (2014) 467-476.
[63] P. Oleszczuk, W. Ćwikła-Bundyra, A. Bogusz, E. Skwarek, Y.S. Ok, Characterization of nanoparticles of biochars from different biomass, Journal of Analytical and Applied Pyrolysis 121 (2016) 165-172.
[64] B.B. Uzun, A.E. Pütün, E. Pütün, Composition of products obtained via fast pyrolysis of olive-oil residue: Effect of pyrolysis temperature, Journal of Analytical and Applied Pyrolysis 79(1-2) (2007) 147-153.
[65] K. Sun, M. Keiluweit, M. Kleber, Z. Pan, B. Xing, Sorption of fluorinated herbicides to plant biomass-derived biochars as a function of molecular structure, Bioresource technology 102(21) (2011) 9897-9903.
[66] K. Wiedner, C. Rumpel, C. Steiner, A. Pozzi, R. Maas, B. Glaser, Chemical evaluation of chars produced by thermochemical conversion (gasification, pyrolysis and hydrothermal carbonization) of agro-industrial biomass on a commercial scale, Biomass and Bioenergy 59 (2013) 264-278.

[67] R.K. Sharma, J.B. Wooten, V.L. Baliga, X. Lin, W.G. Chan, M.R. Hajaligol, Characterization of chars from pyrolysis of lignin, Fuel 83(11-12) (2004) 1469-1482.
[68] J. Cai, W. Wu, R. Liu, Sensitivity analysis of three-parallel-DAEM-reaction model for describing rice straw pyrolysis, Bioresource technology 132 (2013) 423-426.
[69] M. Becidan, G. Várhegyi, J.E. Hustad, Ø. Skreiberg, Thermal decomposition of biomass wastes. A kinetic study, Industrial & engineering chemistry research 46(8) (2007) 2428-2437.
[70] A.s. Anca-Couce, A. Dieguez-Alonso, N. Zobel, A. Berger, N. Kienzl, F. Behrendt, Influence of heterogeneous secondary reactions during slow pyrolysis on char oxidation reactivity of woody biomass, Energy & fuels 31(3) (2017) 2335-2344.
[71] F. Xu, J. Yu, T. Tesso, F. Dowell, D. Wang, Qualitative and quantitative analysis of lignocellulosic biomass using infrared techniques: a mini-review, Applied energy 104 (2013) 801-809.
[72] S. Wang, G. Dai, H. Yang, Z. Luo, Lignocellulosic biomass pyrolysis mechanism: a state-of-the-art review, Progress in Energy and Combustion Science 62 (2017) 33-86.
[73] P. Lv, G. Almeida, P. Perré, Torrefaction of cellulose: Validity and limitation of the temperature/duration equivalence, BioResources 7(3) (2012) 3720-3731.
[74] I. Milosavljevic, V. Oja, E.M. Suuberg, Thermal effects in cellulose pyrolysis: relationship to char formation processes, Industrial & Engineering Chemistry Research 35(3) (1996) 653-662.
[75] K. Kwiatkowski, K. Bajer, A. Celińska, M. Dudyński, J. Korotko, M. Sosnowska, Pyrolysis and gasification of a thermally thick wood particle–Effect of fragmentation, Fuel 132 (2014) 125-134.
[76] J. Akhtar, N.S. Amin, A review on operating parameters for optimum liquid oil yield in biomass pyrolysis, Renewable and Sustainable Energy Reviews 16(7) (2012) 5101-5109.
[77] G. Várhegyi, B. Bobály, E. Jakab, H. Chen, Thermogravimetric study of biomass pyrolysis kinetics. A distributed activation energy model with prediction tests, Energy & Fuels 25(1) (2011) 24-32.

Appendix

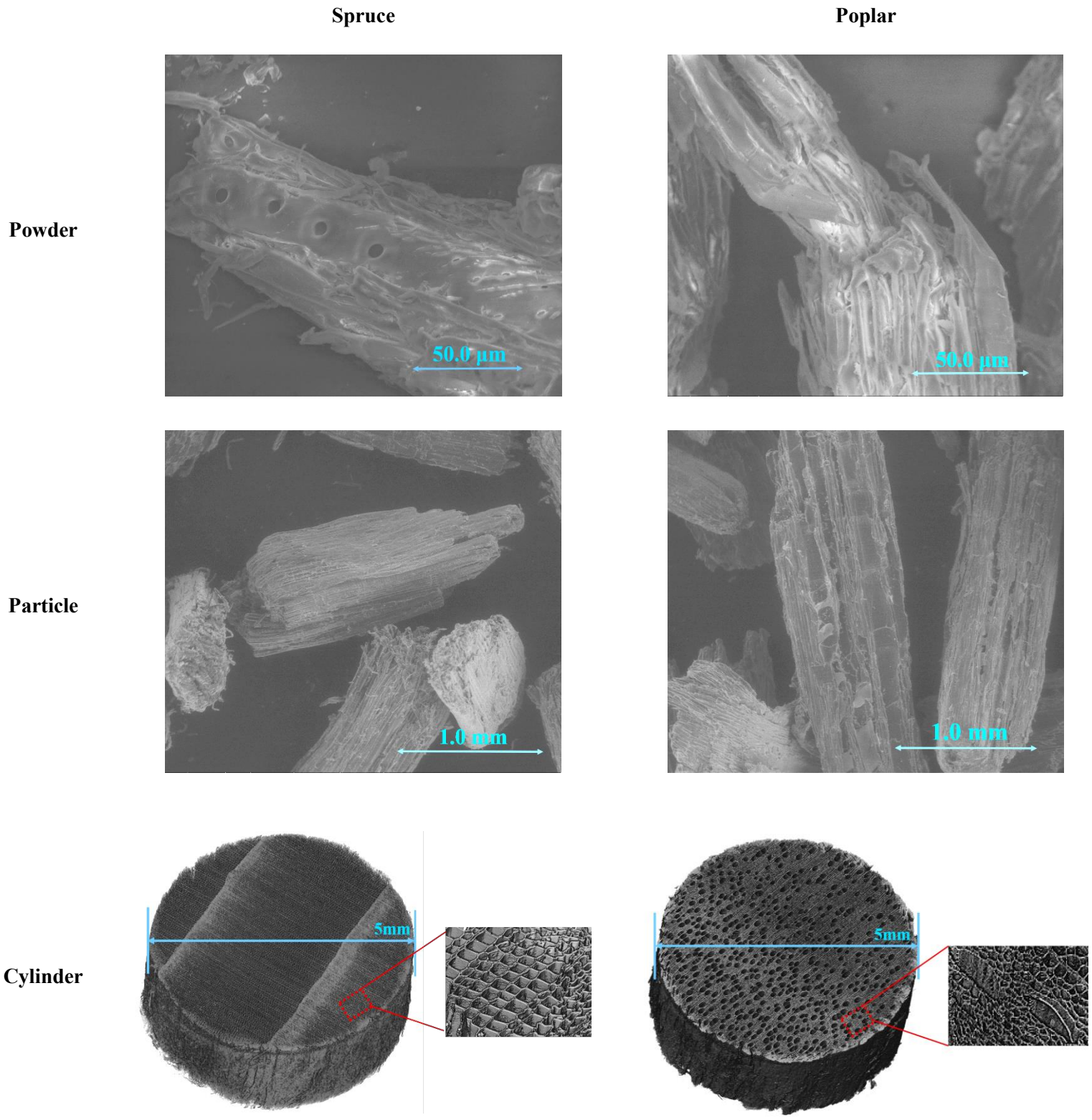

Supplementary Figure 1. SEM images of biomass powder and particles, tomographic images of cylinders (spatial resolution: 3µm) of spruce (first column) and poplar (second column)

4

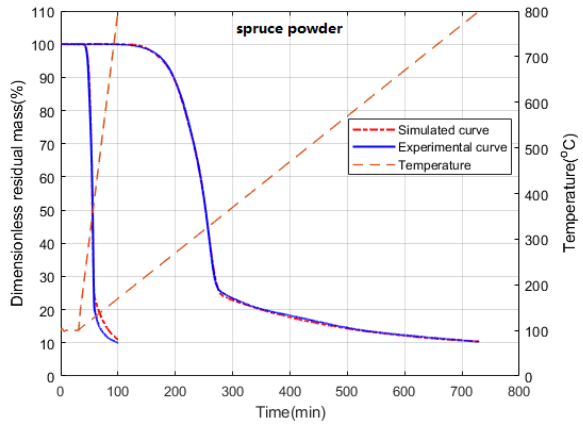
spruce powder
Simulated curve
Experimental curve
Temperature
Dimensionless residual mass(%)
Temperature(°C)
Time(min)

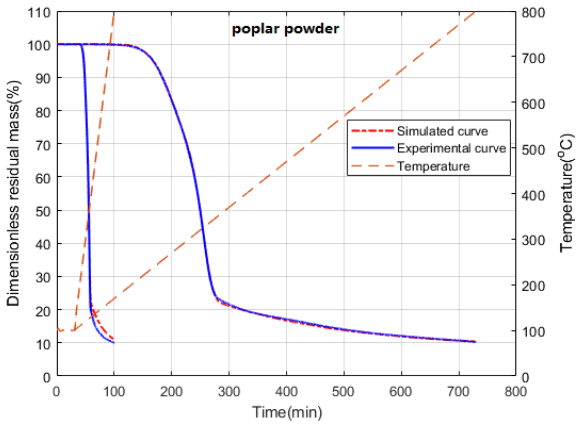
poplar powder
Simulated curve
Experimental curve
Temperature
Dimensionless residual mass(%)
Temperature(°C)
Time(min)

5

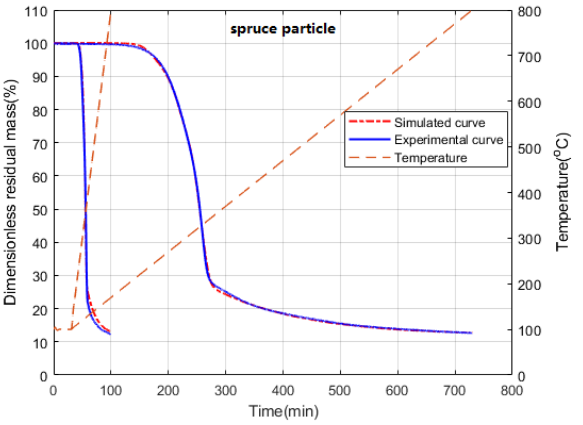
spruce particle
Simulated curve
Experimental curve
Temperature
Dimensionless residual mass(%)
Temperature(°C)
Time(min)

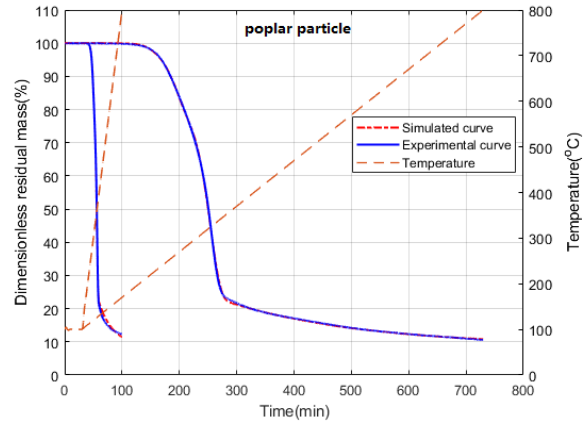
poplar particle
Simulated curve
Experimental curve
Temperature
Dimensionless residual mass(%)
Temperature(°C)
Time(min)

6

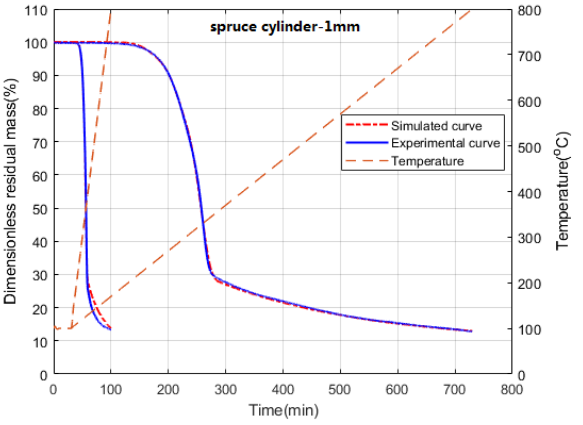
spruce cylinder-1mm
Simulated curve
Experimental curve
Temperature
Dimensionless residual mass(%)
Temperature(°C)
Time(min)

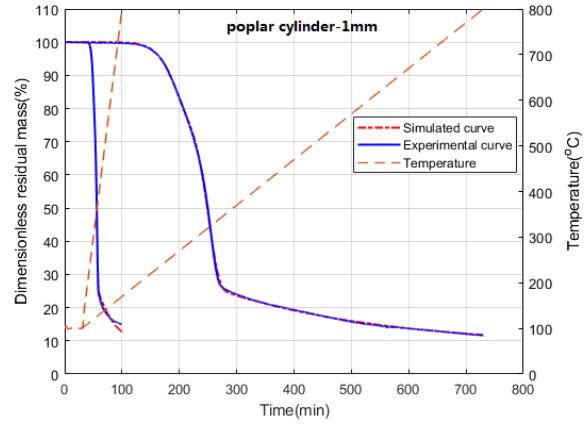
poplar cylinder-1mm
Simulated curve
Experimental curve
Temperature
Dimensionless residual mass(%)
Temperature(°C)
Time(min)

7

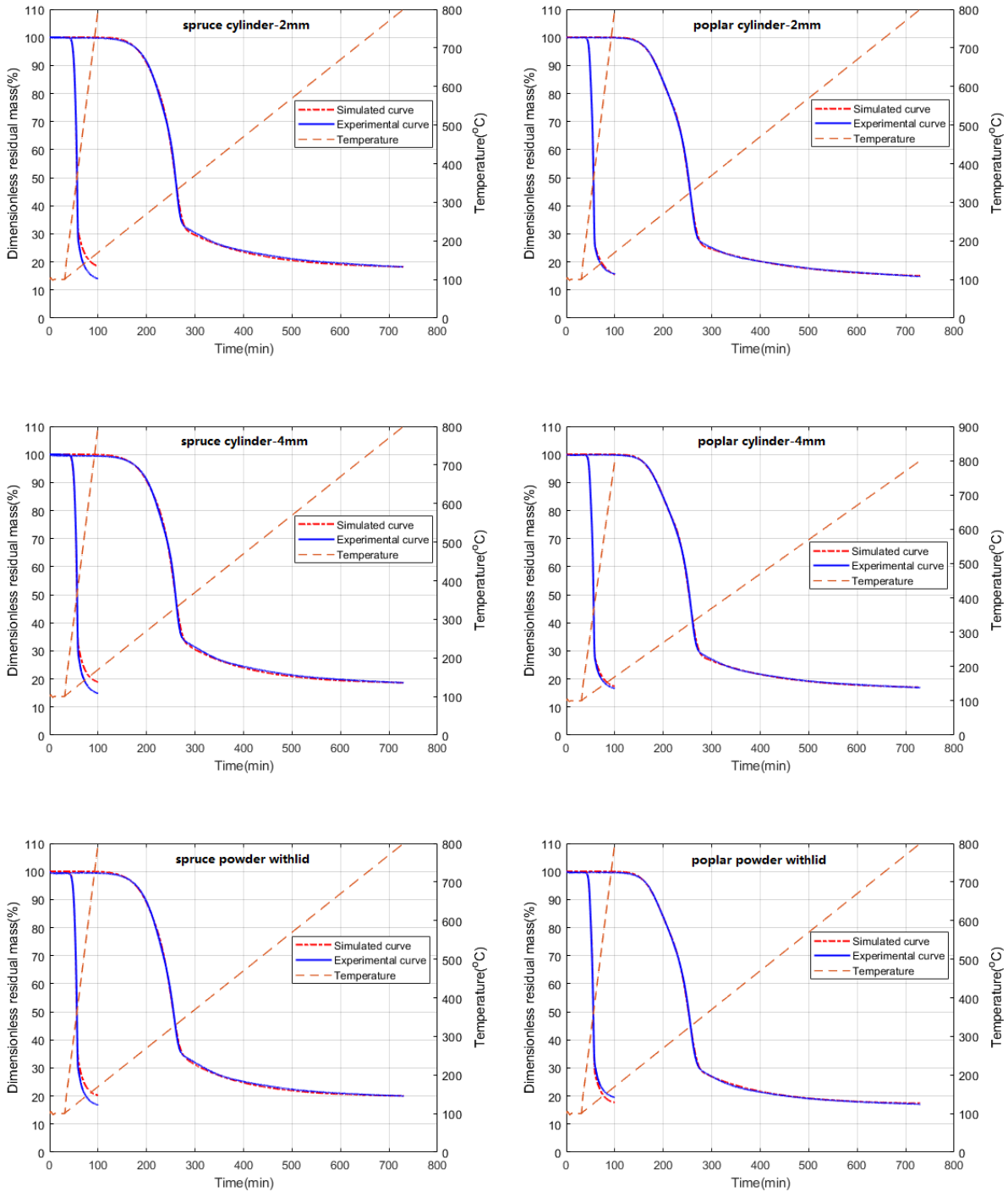

Supplementary Figure 2. Thermogravimetric DRM curves of experiments and model simulations at different sample conditions of spruce (left column) and poplar (right column)

Pseudo-component	Spruce	Poplar
First	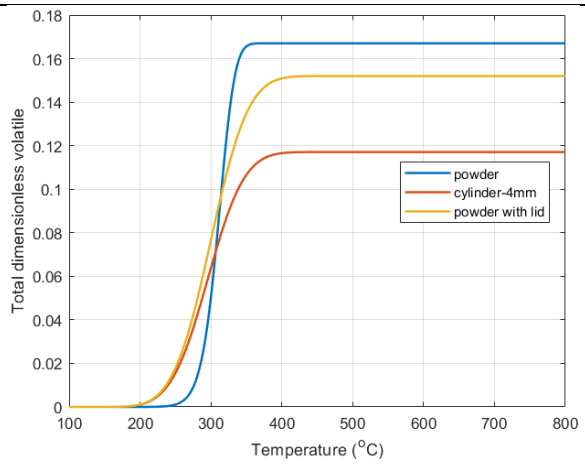	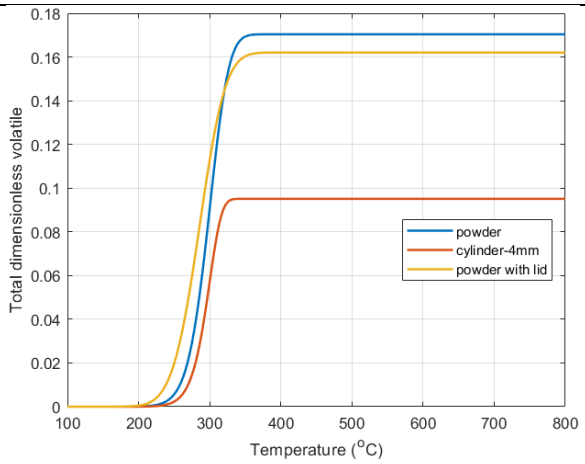
Second	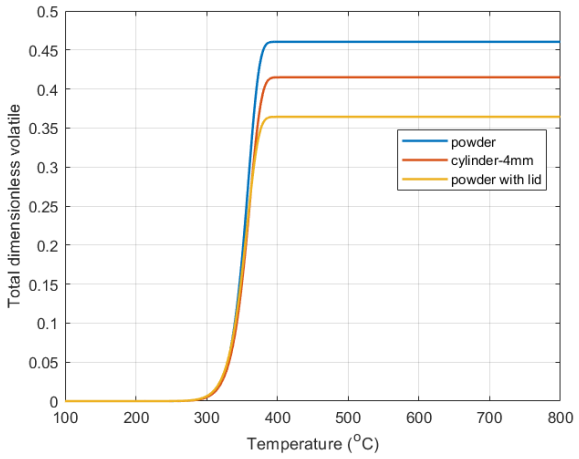	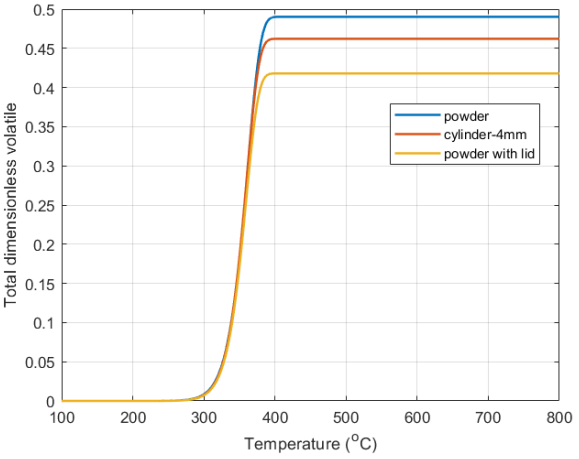
Third	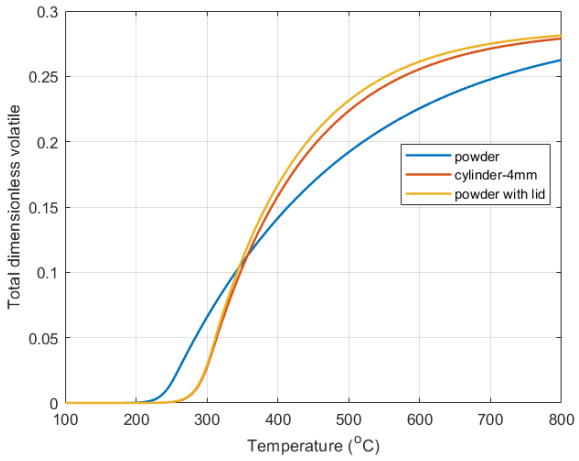	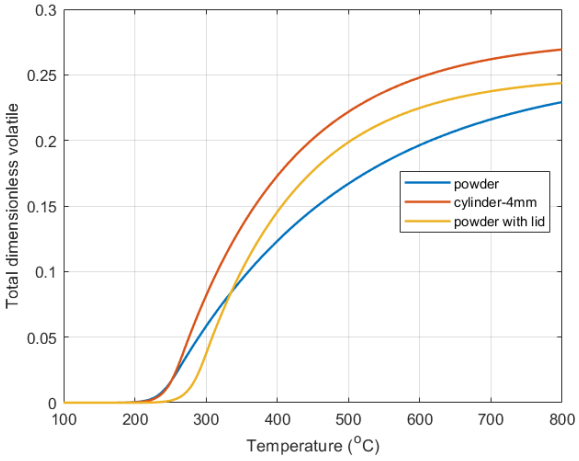

Supplementary Figure 2. Devolatilization profiles of three pseudo-components in 10 °C /min tests of powder, 4-mm cylinder, and powder with lid, computed from the identified model parameters for spruce and poplar

Devolatilization of the first pseudo-component generally occurred between 163–355 °C; it corresponded to the hemicelluloses that were more reactive at lower temperatures [1], in agreement with similar temperatures reported in the literatures [2, 3]. The narrow pyrolytic range and high volatile yield of the second pseudo-component closely matched cellulose, which made up the largest portion of the wood and decomposed at a specific narrow temperature range around 320 °C [4-6]. The temperature of the third pseudo-component had the largest range, from 180 to 800 °C, which was consistent with lignin decomposition characteristics, in which irregular phenolic polymers endowed extended decomposition ranges [7].

Among the three sample types, major differences caused by secondary charring were clearly distinguished by the devolatilization profiles of the pseudo-components. Accompanied by the enlargement of particle size and the use of lid, the first and second pseudo-components reduced their volatile formation rates and final yields, possibly due to the volatile interceptions in hemicellulose and cellulose fractions. On the other hand, the higher volatile content in the third pseudo-component of cylinder-4mm and powder with lid, could be caused by the predominance of lignin devolatilization at high temperatures that raised gas formation rate [8]

Supplementary Table 1. Atomic O/C, H/C ratios and corresponding DML values in dynamic tests with different particle sizes of spruce and poplar

Wood type	Particle condition	1 °C /min			10 °C /min		
		O/C	H/C	DML(%)	O/C	H/C	DML(%)
Spruce	powder	0.032	0.20	89.69	0.032	0.24	90.00
	particle	0.027	0.15	87.36	0.029	0.18	87.70
	cylinder, 1mm	0.026	0.16	87.18	0.028	0.15	86.65
	cylinder, 2mm	0.026	0.12	81.76	0.027	0.14	86.09
	cylinder, 4mm	0.025	0.12	81.33	0.023	0.15	85.18
	powder with lid	0.023	0.11	79.97	0.019	0.12	83.22
Poplar	powder	0.037	0.16	89.73	0.037	0.17	89.99
	particle	0.034	0.15	89.41	0.035	0.18	87.67
	cylinder, 1mm	0.033	0.15	88.39	0.034	0.17	85.07
	cylinder, 2mm	0.033	0.15	85.20	0.032	0.15	84.34
	cylinder, 4mm	0.029	0.13	83.08	0.032	0.14	83.34
	powder with lid	0.027	0.13	82.90	0.031	0.13	80.50

Supplementary Table 2. Elemental analyses of char in static tests of wood powder

	spruce powder						poplar powder					
Temperature (°C)	250	300	350	400	450	500	250	300	350	400	450	500
C (wt.%)	50.77	65.26	71.01	74.28	79.22	82.67	50.30	62.28	70.90	74.44	77.11	81.50
H (wt.%)	5.70	4.27	3.09	3.05	3.11	2.88	5.65	4.75	3.23	2.86	2.87	2.63
O (wt.%)	39.69	24.53	19.19	15.24	12.42	9.49	40.10	28.32	19.99	16.44	13.21	9.62

Reference

[1] P. McKendry, Energy production from biomass (part 1): overview of biomass, Bioresource technology 83(1) (2002) 37-46.
[2] S.D. Stefanidis, K.G. Kalogiannis, E.F. Iliopoulou, C.M. Michailof, P.A. Pilavachi, A.A. Lappas, A study of lignocellulosic biomass pyrolysis via the pyrolysis of cellulose, hemicellulose and lignin, Journal of analytical and applied pyrolysis 105 (2014) 143-150.
[3] S. Wang, X. Guo, K. Wang, Z. Luo, Influence of the interaction of components on the pyrolysis behavior of biomass, Journal of Analytical and Applied Pyrolysis 91(1) (2011) 183-189.
[4] D. Mohan, C.U. Pittman Jr, P.H. Steele, Pyrolysis of wood/biomass for bio-oil: a critical review, Energy & fuels 20(3) (2006) 848-889.
[5] F. Shafizadeh, Pyrolytic reactions and products of biomass, Fundamentals of thermochemical biomass conversion, Springer1985, pp. 183-217.
[6] P. Lv, G. Almeida, P. Perré, TGA-FTIR analysis of torrefaction of lignocellulosic components (cellulose, xylan, lignin) in isothermal conditions over a wide range of time durations, BioResources 10(3) (2015) 4239-4251.
[7] S. Wang, B. Ru, H. Lin, W. Sun, Z. Luo, Pyrolysis behaviors of four lignin polymers isolated from the same pine wood, Bioresource technology 182 (2015) 120-127.
[8] C. Di Blasi, Modeling chemical and physical processes of wood and biomass pyrolysis, Progress in energy and combustion science 34(1) (2008) 47-90.